Eindhoven University of Technology

MASTER

Pressure fluctuations and acoustic force source term due to water flow through an orifice

Roumen, L.

Award date:
2021

Link to publication

ASML TU/e EINDHOVEN UNIVERSITY OF TECHNOLOGY

Department of Mechanical Engineering
Energy Technology Research Group

Pressure fluctuations and acoustic force source term due to water flow through an orifice

Master Thesis

L. Roumen

Graduation Committee:
prof. dr. ir. D.M.J. Smeulders
dr. ir. G. Nakiboğlu
dr. ir. N.P. Waterson
dr. ir. L. Pel

Eindhoven, February 2021

Abstract

Single-hole orifices are often used for measuring flow rate or controlling the static pressure in cooling water pipes. However, these orifices disturb the flow in the pipes and cause flow induced vibrations (FIV) which travel through the cooling circuit. These disturbances are carried over from the fluid domain to the structural domain. For ASML these structural vibrations can cause inaccuracies in the electrical structures on the wafers. In this study the effects of orifice thickness and porosity on pressure fluctuations are investigated, as well as the flow phenomena responsible for the pressure fluctuations. Large eddy simulations (LES) and measurements are performed to accomplish this.

Previous studies have shown that for low mach numbers the noise generation responsible for vibrations travelling through the system can be described by force fluctuations in time. These forces are difficult to measure, but using LES this force source term can be extracted. In the current research LES and measurements are performed for pipe flow with orifice restrictions of various thicknesses and porosities.

The LES and measurements both show that for different orifices of the same porosity that qualify as thick, there is no noticeable difference in produced pressure fluctuations. With the LES it is found that for thick orifices the flow reattaches within the orifice, before expanding at the outlet of the orifice. This results in less vortex structures downstream of the orifice and thus a reduction in the acoustic force generated by the orifice.

It is found that in order to compare the simulations to the measurements, the pressure transducer surface area should be taken into account. The pressure transducer surface area causes surface averaging when measuring small flow structures. This effect is mostly noticeable for frequencies above 600 Hz. Accounting for this effect, a good collapse is found between the measurements and simulations of pressure fluctuations. It is also concluded that measurements under predict local maximum pressure fluctuations due to the surface averaging. The LES and measurements both show that for orifices of a larger porosity, larger pressure fluctuations are observed per unit pressure drop. Similarly, it is observed that thick orifices generally produce less pressure fluctuations than thin orifices per unit pressure drop.

Contents

List of Figures

List of Tables

Chapter 1

Introduction

ASML is the largest supplier of photolithography systems in the world. The machines manufactured by ASML are used worldwide to produce integrated circuits such as computer chips. ASML is constantly developing and improving their Extreme Ultraviolet Lithography (EUV) machines, which allows them to manufacture computer chips with structures as small as 13 nm. Reducing the size of these structures decreases the distance the electrical signals have to travel and increases the amount of structures that can be made per area, which in turn increases the performance of the manufactured chip.

In order to create these structures on a wafer, a high energy laser is focused on microscopic droplets of molten tin to produce a plasma, which emits EUV light. The EUV light is collected using a collector mirror and reflected through additional mirrors to the reticle. The reticle contains a mask which acts as a blue print for the structures that are reflected onto the wafer. The waferstage is where the wafertables are located, which hold the wafers. Two wafers are present in the machine at the same time. One is being measured to optimize alignment and one is exposed to the EUV light. The wafers are moved around electromagnetically on the wafertable, allowing accurate, frictionless positioning at accelerations up to 7G. The inner workings of the EUV lithography machine are depicted in Figure 1.1.
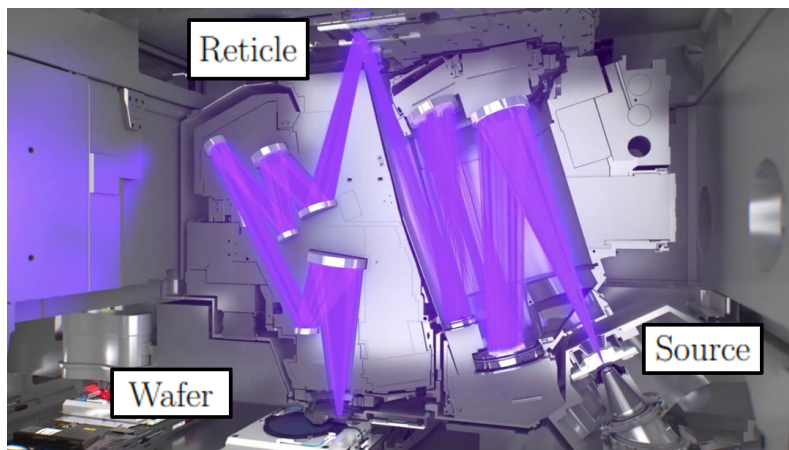
Figure 1.1: EUV light projected on the wafer inside the EUV lithography machine

A lithography machine can have a power consumption of more than 100KW. Only a limited part of this energy is actually used to to project patterns on the wafers and to make the various parts in the machine work. A large portion of the power that is consumed is dissipated in the

form of heat. Heating of the mirrors can cause them to deform due to thermal expansion, which can greatly influence the accuracy of the EUV light beam. This in turn results in less accurate structures in the chips, which is very undesirable.

Preventing this unwanted thermal expansion of mirrors and other components is done by using Liquid Cooling Water (LCW) lines. More than 100 liters of water are pumped through the lithography machine each minute for cooling purposes. The water is pumped though various bends and components in the system. Orifices are commonly used as flow control devices, providing flow balancing or pressure drops where needed. However, interactions between the cooling water and these bends, orifices and other components cause pressure disturbances. These pressure disturbances can travel a long distance through the LCW lines [7] and cause flow induced vibrations (FIV) to mechanical parts of the system [8]. Figure 1.2 schematically displays the interactions of noise generating components and mechanical components in the system.
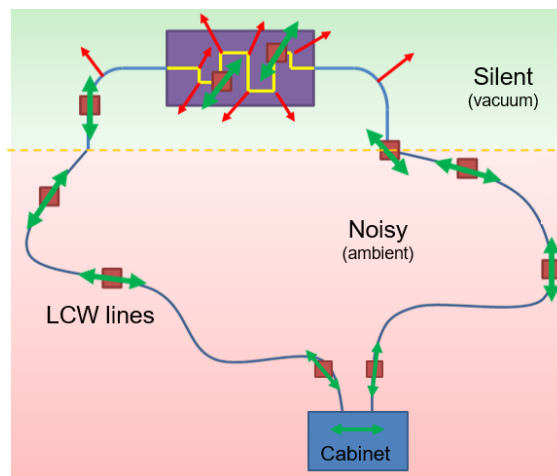
Figure 1.2: Liquid water cooling system containing a sensitive and non-sensitive region. The brown squares indicate components which generate flow disturbances (green arrows). The resulting excitations on the LCW pipes are indicated by the red arrows. [1]

As the electrical structures on the chips keep becoming smaller, the accuracy of the manufacturing becomes increasingly important. The flow induced vibrations must therefor be taken into consideration in order to retain maximum accuracy.

1.1 Motivation

The main topic in this research is the FIV due to fluid flow through an orifice. More specifically the influence of the orifice thickness on pressure fluctuations is examined. Through experiments conducted at ASML [9] it was found that thick orifices perform better in terms of pressure fluctuations per unit pressure drop than thin orifices. It is hypothesized that the lower pressure fluctuations for thick orifices occur due to the flow reattaching within the orifice before reaching the outlet of the orifice, stabilizing the flow and not causing as large pressure fluctuations. In order to gain a better understanding of the flow phenomena responsible for the pressure fluctuations in the system and orifice flow in general, computational fluid dynamics (CFD) programs can be used to do fluid simulations. Large eddy simulations (LES) show promising results for transient simulations [1]. Parallel to the simulations, experiments can be carried out to validate the results obtained from LES and gain more knowledge on near field and far field pressure fluctuations.

Continuing on work by Moonen [9] and Krabben [1], orifice flow and the associated acoustic disturbances are investigated. The goal of the present investigation is to use LES as a means of

extracting a source term. From this source term far field pressure fluctuations can be predicted. Secondly, an attempt is made to find the flow phenomena responsible for the FIV caused by orifices.

1.2   Thesis outline

A research approach is proposed to investigate the influence of the orifice thickness on pressure fluctuations in the system and the corresponding source term. Figure 1.3 shows a block diagram of the outline of the thesis. In Chapter 2 the relevant theory and previous work on orifice research will be discussed. This includes orifice flow and large eddy simulations in general, as well as relevant experimental and numerical research.

Chapter 3 describes the experimental approach used during this research. A complete overview of the test setup, instrumentation and test conditions is discussed. Subsequently, the way pressure fluctuations are measured and post processing needed to acquire comparable data is explained. In Chapter 4 the numerical approach is explained. The setup of the numerical model using commercial software is discussed. This includes the meshing, boundary conditions and models and solvers used for the LES. Similarly to the experimental approach, the data extraction from the simulation is discussed as well as the analysis of the data.

The experimental results, simulation results and a comparison between the two are evaluated in Chapter 5. For the experimental results pressure measurements are used at near field and far field locations. The simulation results consist of flow fields, near field pressure fluctuations and the force source term are discussed. In Chapter 6 conclusions are drawn from the results discussed in Chapter 5 and recommendations are given for future work on this topic. Lastly the bibliography and Appendix are included.
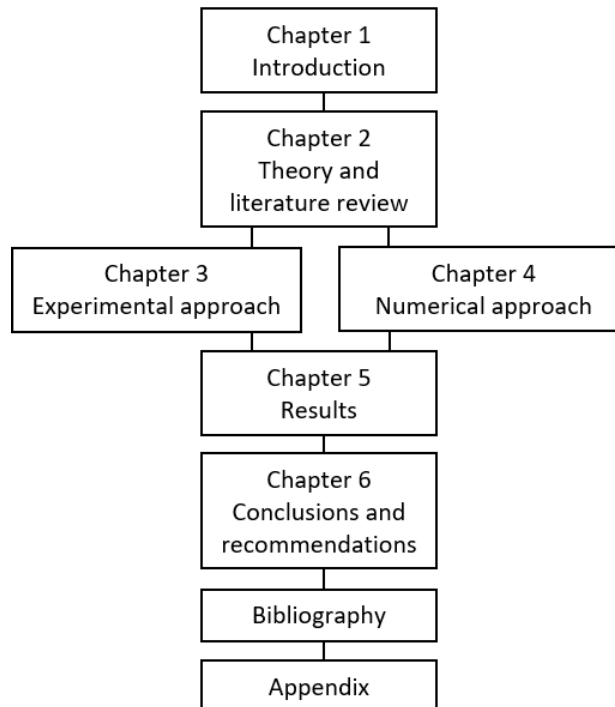
Figure 1.3: Block diagram of the outline of the thesis

Chapter 2

Theory and literature review

In this chapter the theory behind orifice flow, LES and noise generation in general is discussed. Also a look is taken at relevant literature regarding previous work on experiments and simulations on orifices.

2.1 Orifice flow

A single hole orifice plate is often used for measuring flow rates, restricting flow or reducing the static pressure in fluid channels. When a fluid passes through the orifice plate, the pressure slightly upstream of the orifice increases. Then, as the fluid passes through the orifice itself the velocity of the fluid increases due to conservation of mass. The velocity keeps increasing downstream of the orifice until it reaches the vena contracta, where the velocity of the jet is the highest and the pressure is the lowest. The static pressure further downstream is then partly recovered and a permanent pressure loss is induced comparing the upstream and downstream static pressure. The geometry and the flow specifications of flow through an orifice also greatly influence the pressure drop that is induced [10, 3]. Figure 2.1 shows a schematic overview of the flow through a single hole orifice and the associated pressure profile.

(a) Flow profile through a single hole orifice

(b) Typical pressure profile across an orifice plate
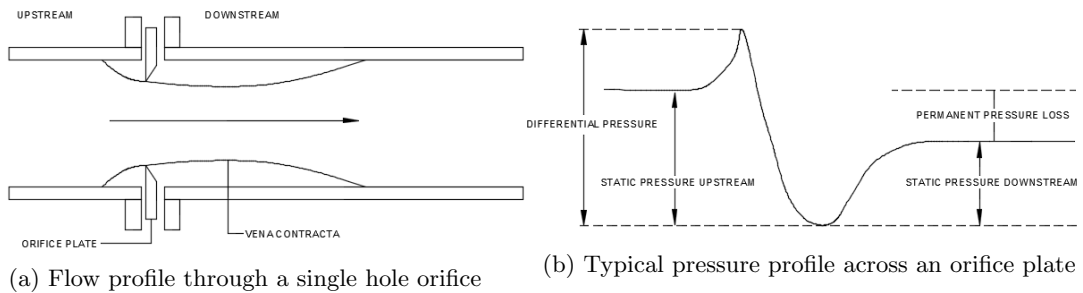
Figure 2.1: Schematic overview of flow through a typical single hole orifice and the associated pressure profile [2]

The pressure drop is found to be a function of the geometry of the orifice as studied by Anantharaman [10]. The maximum pressure drop that can be induced by an orifice as described by Bird et al. [11] is given by:

$$\Delta p_{max} = \frac{1}{C_d} \frac{1}{2} \rho u_b^2 \left(\beta^{-4} - 1 \right).$$

(2.1)

Where C_d is the discharge coefficient, ρ is the fluid density, u_b is the bulk velocity and β is the porosity of the orifice. The porosity of the orifice is expressed by the ratio between the orifice are and pipe area:

$$\beta = \frac{A_o}{A_p} = \frac{d_o^2}{D^2}. \tag{2.2}$$

Here, A_o and d_o are the area and diameter of the orifice respectively. Furthermore, A_p and D are the area and diameter of the pipe respectively. An empirical relation between the permanent pressure drop and the maximum pressure drop can now be described as:

$$\frac{\Delta p_{perm}}{\Delta p_{max}} = 1 - \beta^2. \tag{2.3}$$

Understanding why a pressure drop is induced can be done by looking at the conservation of energy as done by Pope [12]. The energy dissipation rate for incompressible flow through orifices at low Mach numbers is given by:

$$\epsilon = Q\Delta p_{perm} = Q\Delta \left(p + \frac{1}{2}\rho u^2 \right) = \bar{\epsilon} + \epsilon_k, \tag{2.4}$$

where ϵ is the dissipation rate and Q is the volume flow rate. The decrease of mechanical energy should be equal to the increase in internal and turbulent kinetic energy, because conservation of energy holds for a fixed control volume. This is described by Kundu et al. [13] using the following relation:

$$-\iint_{\partial V} \rho u_i \left(\frac{p}{\rho} + \frac{u^2}{2} \right) dS = \iint_{\partial V} \rho u_i (e + k), \tag{2.5}$$

where e is the internal energy and k the turbulent kinetic energy (TKE). The production and dissipation of TKE is what is generating the FIV disturbances. The FIV disturbances then travel through the system towards other components.

2.1.1 Effect of orifice geometry on pressure loss

An empirical relation between the pressure loss coefficient and the geometric properties of an orifice is provided by Idelchik [3]. The relation is based on experiments spanning several years of research and is valid for the flow conditions used in the current study. The relation between the pressure loss coefficient and the geometric properties of an orifice are described by:

$$K = \left(0.5(1-\beta)^{0.75} + \gamma(1-\beta)^{1.375} + (1-\beta)^2 + \left(w \cdot \frac{t_o}{d_o} \right) \right) \left(\frac{1}{\beta} \right)^2, \tag{2.6}$$

where

$$\gamma = (2.4 - t_o/d_o) \cdot 10^{-\phi}, \tag{2.7}$$

and

$$\phi = 0.25 + \frac{0.535 \cdot (t_o/d_o)^8}{0.05 + (t_o/d_o)^7}. \tag{2.8}$$

Here K is the pressure loss coefficient and w is the surface roughness, which is neglected ($w = 0$) as the current study is using smooth pipes. A plot of the loss coefficient as a function of orifice thickness to diameter ratio for several porosities is shown in Figure 2.2.

Figure 2.2 clearly shows that for each of the porosities a thin orifice induces a significantly larger loss coefficient than for a thick orifice. From this plot it can be seen that for a thickness to diameter ratio of $t_o/d_o >= 1.5$ the pressure loss coefficient flattens out which is in agreement with Maynes et al [14]. The pressure loss coefficient is related to the pressure loss using the following equation:

$$K = \left(\frac{\Delta p}{\frac{1}{2}\rho u_b^2} \right), \tag{2.9}$$
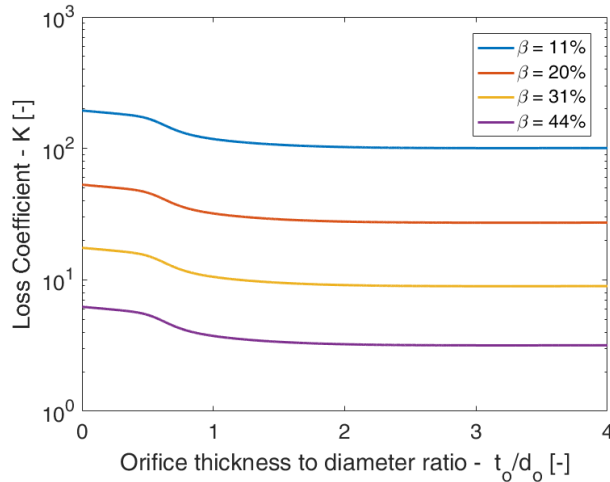
Figure 2.2: Loss coefficient as a function of orifice geometry as described by Idelchik [3]

where Δp is the pressure loss over the region of interest. When measuring the pressure loss over an orifice it should be kept in mind that the pressure downstream should be measured sufficiently far downstream. This ensures that the pressure recovery step is completed and the static pressure downstream is measured.

2.2 Large eddy simulation

In LES a mathematical model is used for modeling turbulence in computational fluid dynamics, initially proposed by Smagorinsky [15] and later explored by Deardorff [16]. Unlike direct numerical simulation (DNS), which resolves a wide range of time and length scales, LES ignores the smallest length scales and models these instead. While DNS would be preferable in terms of resolution, DNS is computationally very expensive and is therefor not a viable method for many simulations [17].

2.2.1 Turbulence

Turbulence can be described as excessive kinetic energy in parts of the fluid flow domain which overcomes the damping induced by the viscosity of the fluid. Turbulent flow is characterised by fluctuating pressure and velocity and plays a large role in the generation of noise and pressure drops. Within turbulent flow vortex structures such as eddies are formed. These eddies are unstable and break up into smaller eddies while losing energy. The break up of eddies is due to vortex stretching and eventually when the eddies become small enough they are dissipated into thermal energy by the viscosity interaction of the fluid molecules [18]. Figure 2.3 shows the eddies breaking up and losing energy as they decrease in size.

Only larger turbulent scales are solved in LES, which means that the smaller scales are modelled. For the modelling these smaller scales a subgrid-scale model (SGS) is used. The SGS model is used to bridge the large energy-containing eddies (l_0) with the smaller eddies (η) where the energy is dissipated. Figure 2.4 shows how the energy is contained for eddies of different sizes.

The smallest turbulent length scales are described by Kolmogorov as [19]:

$$\eta = \left(\frac{\nu^3}{\epsilon} \right)^{1/4} \tag{2.10}$$

Here ν is the kinematic viscosity and ϵ is the turbulence dissipation rate. The Kolgomorov
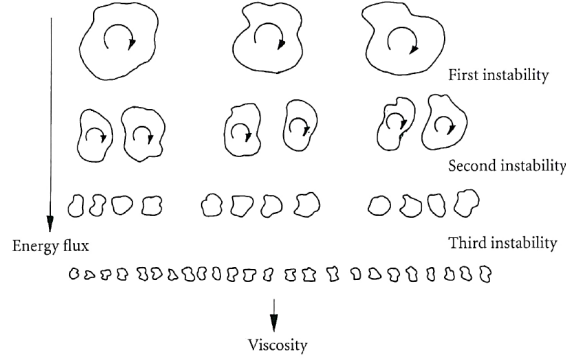
Figure 2.3: Turbulent eddies being converted to smaller eddies and finally to viscosity [4]
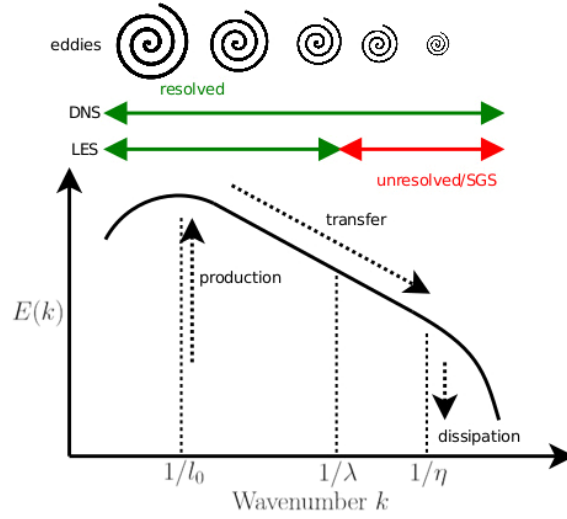
Figure 2.4: Energy contained as a function of eddy size [5]

length scale (η) describes the smallest length scale after which the energy is converted into heat. The large eddies containing the most kinetic energy are characterized by the length scale l_o:

$$l_0 = \frac{k^{\frac{3}{2}}}{\epsilon} \tag{2.11}$$

Here k is the turbulence kinetic energy, which is used to express the amount of kinetic energy present per unit mass. The TKE is defined as the mean kinetic energy per unit mass and can be expressed as half the sum of the variances of the velocity:

$$k = \frac{1}{2} \sum \left(\bar{u'_i}^2 \right), \tag{2.12}$$

where $\bar{u'_i}^2$ is the variance in of the velocity in i-direction. Most of the TKE is present in the energy containing range, which is in the turbulent length scale (TLS) range of $\frac{1}{6} l_0 < l < 6 l_0$. This is where energy is injected into the flow and because the least energy has been dissipated, the eddies here contain the most energy. As the TKE of the eddies decreases the size of the eddies also decrease. The eddies move through the inertial subrange towards the dissipation range which is $60\eta < l < \eta$.

2.2.2 Governing equations

For the large eddy simulations the governing equations are the Navier-Stokes equations, which are a set of partial differential equations which describe the motion of a viscous fluid flow. The Navier-Stokes equations use conservation of mass and Newton's second law ($F = ma$) as their base. It is assumed that the fluid flow is incompressible which results in the following equations for conservation of mass and momentum [20]:

$$\frac{\partial u_i}{\partial x_i} = 0 \tag{2.13}$$

$$\rho \frac{\partial u_i}{\partial t} + \rho u_i \frac{\partial u_i}{\partial x_i} = -\frac{\partial p}{\partial x_i} + \mu \left(\frac{\partial^2 u_i}{\partial x_i^2} + \frac{\partial^2 u_i}{\partial x_j^2} \right) + F_i. \tag{2.14}$$

Where ρ is the fluid density, u_i is the velocity component in i-direction, p is the pressure, μ is the dynamic viscosity and F represents the forces acting on the fluid. Equation 2.14 describes the acceleration on the left hand side and the sum of forces on the right hand side. The forces are split up into a pressure term, is viscous term and a term containing any other internal or external forces. Dividing the momentum equation by the density and rewriting it in viscous terms results in the following equation:

$$\frac{\partial u_i}{\partial t} + u_i \frac{\partial u_i}{\partial x_j} = -\frac{1}{\rho} \frac{\partial p}{\partial x_i} + \left[\nu \left(\frac{\partial^2 u_i}{\partial x_i^2} + \frac{\partial^2 u_i}{\partial x_j^2} \right) \right] + \frac{F_i}{\rho}. \tag{2.15}$$

Where ν is the kinematic viscosity. The part in square brackets on the right hand side of the equations now shows the viscous stress tensor for incompressible fluids, τ_{ij}.

2.3 Noise generation

Lighthill [21] describes that the radiating sound in fluid flow is caused by acoustic quadrupoles. He presented the following non-homogeneous wave equation:

$$\frac{\partial^2 \rho}{\partial t^2} - c^2 \frac{\partial^2 \rho}{\partial x_i^2} = \frac{\partial^2 T_{ij}}{\partial x_i \partial x_j}, \tag{2.16}$$

where T_{ij} is the Lighthill tubrulent stress tensor, defined as:

$$T_{ij} = \rho u_i u_j - \tau_{ij} + (p - c^2 \rho) \delta_{ij}. \tag{2.17}$$

The tensor $\rho u_i u_j$ is called the Reynolds stress and expresses the instensity of the turbulence in the source region. τ_{ij} expresses the viscous part and the term $p - c^2 \rho$ expresses the differential between the actual pressure fluctuations in the ambient fluid medium. It is theorized that the acoustic forces generated by fluid flow can be described as a fluid at rest on which fluctuating stresses are applied. These fluctuating stresses in the fluid flow behave as sound generating quadrupoles.

Powell [22] describes the far field acoustic pressures using the following equation:

$$\begin{aligned}
4\pi p_a(x, t) = & \frac{\partial}{\partial x_i} \iiint_V \frac{[\rho(\boldsymbol{\omega} \times \boldsymbol{u})_i]}{r} dV(y) \\
& + \frac{1}{c_0^2} \frac{\partial^2}{\partial t^2} \iiint_V \left[p - \rho c_0^2 + \frac{1}{2} \rho u^2 \right] \frac{dV(y)}{r} \\
& + \frac{\partial}{\partial x_n} \iint_S \left[p + \frac{1}{2} \rho u^2 \right] \frac{dS(y)}{r} - \iint_S \left[\rho \frac{\partial u_n}{\partial t} \right] \frac{dS(y)}{r}
\end{aligned} \tag{2.18}$$

Equation 2.18 can be explained as the sum of four contributions:

1. a volume distribution of dipoles proportional to $\boldsymbol{\omega} \times \boldsymbol{u}$,

2. a volume distribution of nondirectional sources; $\partial^2 \left(p - \rho c_0^2 + \frac{1}{2}\rho u^2 \right) \partial t^2$,

3. a surface distribution of dipoles, proportional to the Bernoulli pressure on the surface, $p + \frac{1}{2}\rho u^2$,

4. a monopole distribution whose strength is proportional to the acceleration of the normal surface normal to itself, $\partial u_n / \partial t$.

The second volume integral involves quantities of order $(u/c_0)^2$. For low Mach-number flow this term can be neglected.

2.4 Experimental research

The governing Navier-Stokes equations in a fluid flow are non-linear and make it difficult to analytically predict FIV caused by a source [23]. Therefor doing experiments is a viable approach for investigating FIV propagation. The effects of a noise generating component can be measured easily with the use of pressure transducers. The source term itself however cannot be measured directly.

It was found by Agarwal [24] that flow approaching a thin orifice remains undisturbed upstream of the orifice until it gets close to the orifice. He found that the values of the power spectral density (PSD) and the root mean square (RMS) of the pressure in the developed regions downstream and upstream of the orifice were higher than that of normal pipe flow. He attributed the difference to propagating acoustic waves generated by the flow disturbance produced by the orifice plate. It was also found that the overall wall pressure fluctuations are a function of the maximum mean flow velocity. It should be noted that the experiments conducted by Agarwal used air as the fluid medium.

Qing et al. [25] performed experiments using a thin orifice and water as a fluid medium. They found that the pipe flow experienced greatly increased pressure fluctuations when using a flow restricting orifice. They also found that the bulk of the turbulent kinetic energy caused by near field turbulence is concentrated in the low frequency range. It was found that highest fluctuating pressure level was located 1.7 pipe diameters downstream of the orifice in axial direction, while the PSD and RMS of the pressure fluctuations did not show significant difference in the radial direction.

Experiments by Anantharaman [10] showed that the length of the recirculation regions downstream of the orifice are a function of the orifice geometry. He also found that for single-hole and multi-hole orifices of the same porosity and thickness to diameter ratio comparable pressure losses can be achieved. Also a whistling behaviour was found for cavitating single-hole orifices at $St \approx 0.2$. Similar to Qing et al., the pressure fluctuations downstream of the orifice were found to be proportional with the square of the incoming flow speed. They also found that the location of the peak pressure fluctuations was within $0 - 2D$ from the orifice.

Attempts are made to scale the source term and broadband turbulent noise in general by Moussou [26], Violato, de Jong and Golliard [27]. They found that scaling methods based on pressure drop, momentum flux and surface acoustic intensity were successful.

2.5 Numerical research

According to Moore's law [28] the capability of computers increases exponentially. As computing power has been increasing over the years, CFD has become more computationally affordable and a viable resource for flow research [29]. Even though full scale DNS is still outside of the scope

of everyday simulations, LES and simulations using Reynolds-Averaged Navier-Stokes (RANS) equations are a viable option, as DNS is not required in most cases [17].

Using RANS simulations, Sibe et al. [30] found that the velocity profile, differential pressure and vorticity of the flowing fluid inside the pipe and around the orifice can accurately be described. Simulations were carried out for several orifice porosities and at several Reynold numbers.

LES of flow through a thick orifice plate has been conducted by Alenius [31], using air as the fluid flow. A good match was found between experimental data and data extracted from LES. It was found that the main mechanisms for generating plane wave sound were the fluctuating mass flow at the orifice openings and a fluctuating force at the plate sides, for subsonic jets.

Benhamadouche et al. [32] conducted LES for a thin orifice. They used mesh sizing based on preliminary RANS results. They used a recycling method as the inlet condition, which consists of straight pipe with periodic boundary conditions. Good agreement for the pressure loss and discharge coefficient was found when comparing to experiments and their overall conclusion was that wall-resolved LES is highly accurate in simulating the flow across a square-edged orifice. Krabben [1] did research on the mesh sizing and setup of LES. He concluded that the recycling method is the easiest and best to generate turbulence at the inlet of the domain. No accurate initial information is required to use this method. The proposed setup that was created was found suitable to study the characteristics of the sound force.

Chapter 3

Experimental approach

In order to determine the effects of orifices in straight pipe flow, a test setup is devised. This test setup resembles the real world application in the EUV machines, but greatly simplified. In this chapter first the way the measurements were setup is explained. Then it is discussed how measurements were taken and how the data obtained from the measurements is post processed.

3.1   Test setup

The experimental setup is based on the previously devised setup as explained in the work of Anantharaman [10]. A new orifice mount is machined allowing for thin as well as thick orifices to be mounted in the setup. A further explanation and the technical drawings of the new orifice mount can be found in Appendix A. The schematic overview of this setup can be found in Figure 3.1. Here the thick black lines represent the hard ducted parts of the test setup and the thin black lines represent the tubes used to connect different components of the water system.
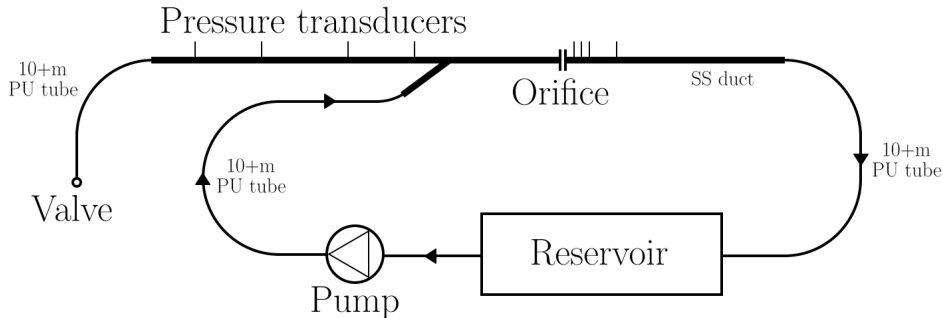
Figure 3.1: Schematic overview of the experimental setup

Demineralized water is used within the system and is pumped through polyurethane (PU) tubes to the test section. The test section consists of smooth stainless steel (SS) ducts with a total length of approximately 3000 mm. The orifice mount section, the Y-splitter and pressure sensor mounting blocks are made of aluminium. All tubes, ducts and other components have an inner diameter of $D = 9$ mm. Sensor mounting blocks were manufactured and used to mount the pressure transducers at any location in the system. A Y-splitter is included in the setup in order to have no flow at the far field pressure measurements. The Y-splitter has an angle of 30° with the rest of the ducts and is used instead of a T-splitter in order to minimize the amount of acoustic forces generated by the sudden bend. This way the pressure fluctuations measured will be predominantly caused by acoustic forces and not by hydrodynamic forces. SS ducts of various lengths were used to place the sensor mounts at the desired locations. All parts of the system were

connected using nut connections and straight couplings. The side branch with the far field pressure sensors is connected to a PU tube, filled with water and closed off at the end using a ball valve.

Holes are included in the orifice mount so pressure transducers can be flush mounted to the inner walls at axial distances $x/D = 1, 2, 3, 6$ from the orifice. The sensor holes were placed in those positions because this is where the largest pressure fluctuations are expected [25]. A photo of the orifice mount setup in the system can be seen in Figure 3.2.
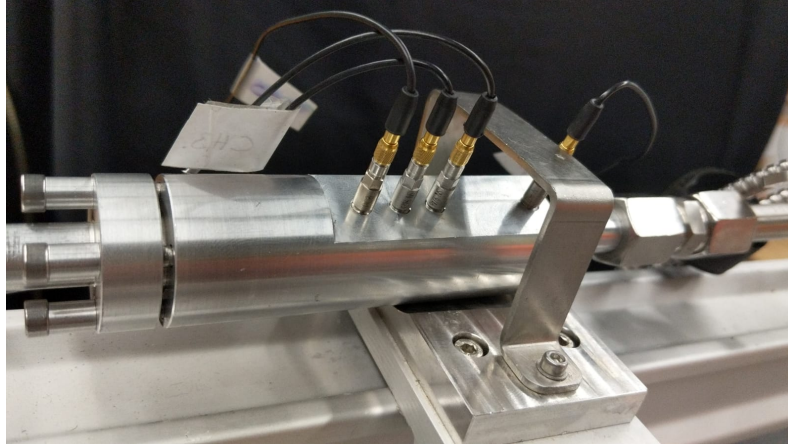
Figure 3.2: Photo of the new orifice mount as used in the experiments

3.1.1 Pressure transducers

Pressure measurements were done using PCB Piezotronics 105C02 ICP® [33]. The pressure transducers use two quartz discs in a thickness compression mode which generate a signal that is amplified within the sensor housing. The sensors have a stainless-steel housing with a sensing element diameter of 2.5 mm and can be connected directly into most common readout instruments using a coaxial connector. Table 3.1 shows the specifications of the pressure transducers used as specified by the manufacturer.

Table 3.1: Specifications of the PCB Piezotronics 105C02 ICPICP® as reported by the manufacturer

Property	Value
Sensitivity	7.3 mV/kPa
Maximum Pressure	1720 kPa
Resolution	0.035 kPa
Resonant frequency	$\geq$ 250 kHz
Rise time	$\leq$ 2 µsec
Operating temperature range	-73°C to +121 °C

3.1.2 Differential pressure meter

A differential pressure meter is used to measure the pressure drop over a length of pipe and the static pressure drop over an orifice. The device used in the setup is the Wöhler DC 2000^{PRO} Pressure Computer. The specifications of the pressure meter can be found in Table 3.2.

Table 3.2: Specifications of the Wöhler DC 2000^{PRO} Pressure Computer as reported by the manufacturer

Property	Value
Measurement range	± 2 bar
Dimensions	1754 x 165 x 52 mm
Accuracy	<3 %
Operating temperature	-5 - 60 °C
System	Piezoresistive

3.1.3 Pump

The pump used in the setup is a compact magnetically coupled gear pump made by Suurmond. This kind of pump is pulsation free and produces accurate and reproducible mass flow. The pump uses one DC permanent magnet motor. It is connected to the system via PU tubing which help reduce the acoustic noise generated by the pump. The pump is hermetically sealed using O-rings and the housing is made of stainless steel. The specifications as reported by the manufacturer can be found in Table 3.3.

Table 3.3: Specifications of the compact magnetically coupled pump as reported by the manufacturer

Property	Value
Drive speed	350-6000 RPM
Maximum volume flow	5.8 l/min
Operating temperature	0 - 40 °C
External control voltage	0 - 10 V

3.1.4 Flow meter

A FLEXIM FLUXUS F601 Ultrasonic Flow (USF) meter is used to measure the flow velocity in the test setup. This flow meter is chosen because it is non-intrusive and works by clamping two transducers to a SS pipe in the system. Ultrasonic signals are transmitted from one transducer, reflected by the pipe wall and received by the other transducer, alternating with and against the flow direction (see Figure 3.3a). The transit time of the ultrasonic signal in flow direction is shorter than the one against the flow direction. The time difference between these transit times is what allows the flowmeter to determine the average flow velocity (Figure 3.3b). The specifications of the flowmeter can be found in Table 3.4.
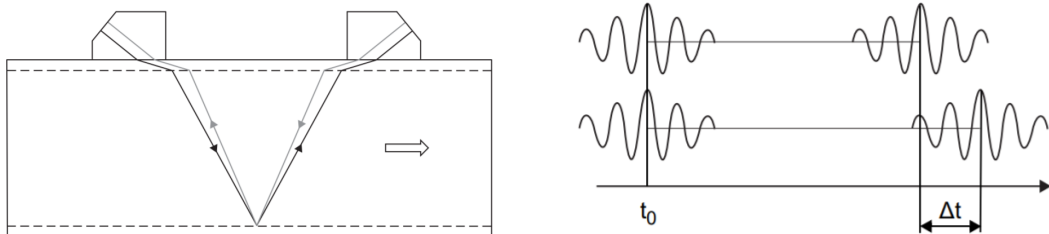
(a) Path of the ultrasonic signal in the flowing fluid   (b) Transit time difference Δt

Figure 3.3: Schematic representation of the working principle of the ultrasonic flow meter [6]

Table 3.4: Specifications of the FLUXUS F601 ultrasonic flow meter as reported by the manufacturer

Property	Value
Measurement range	0.01 - 25 m/s
Repeatability	<0.15% of measured value
Accuracy	<0.5% of measured value
Response time	1 s

3.1.5 Data acquisition

Data acquisition is done by first running the signals from the pressure transducers through an amplifier to a PicoScope® 4824 using coaxial cables. The PicoScope® 4824 is a high resolution, deep memory, 8 channel oscilloscope. The specifications of the PicoScope can be found in Table 3.5. The signals are then ran from the oscilloscope through a USB 3.0 cable to a computer. The signals can then be logged and manipulated using the PicoScope software. Within the software the calibration profile of each pressure transducer is used to get a direct pressure measurement. The data acquired through PicoScope can then easily be saved to later be used for post processing using MATLAB.

Table 3.5: Specifications of the PicoScope® 4824 as reported by the manufacturer

Property	Value
No. channels	8
Resolution	12 bit
Bandwidth	20 MHz
Buffer memory	256 MS
Sample rate	80 MS/s

3.1.6 Orifice geometries

In order to investigate the influence of the thickness to hole diameter ratio of an orifice on the pressure fluctuations, multiple orifice geometries were tested. Measurements are taken in the near field and far field from the source. The geometries of orifices used can be found in Table 3.6.

Table 3.6: Geometries of the single-hole orifice plates used in the experimental setup

Plate number	Orifice diameter d_o (mm)	Plate thickness t_o (mm)	Porosity β (%)	Thickness ratio t_o/d_o (-)
1	4	2	20	0.5
2	4	4	20	2
3	4	8	20	4
4	5	2.5	31	0.5
5	5	5	31	2
6	5	10	31	4

The thickness ratio's were chosen in such a way that a comparison can be made between thick and thin orifices of the same porosity. The transition between thin and thick orifice is estimated as $t_o/d_o \approx 1.5$ [14]. Because simulations and experimental results of the thin orifice were available through Kottapalli [34], it was chosen to match the porosity of the thick orifices to that of the earlier work.

3.2 Pressure measurements and post processing

Before each measurement, water was ran through the circuit for at least 5 minutes with the side branch open to ensure that the flow was stabilized. The water circuit was also checked for any air bubbles. After all the tubing and ducting was filled with water, the side branch was closed off using a ball valve. Pressure measurements were then carried out at a sampling frequency of 100 kHz over a time of 120 seconds using the pressure transducers and the PicoScope interface as described in Section 3.1.5. The fluctuating component of the pressure time signal can then be obtained using Reynolds decomposition. Reynolds decomposition splits the original signal into a mean part and a fluctuating part:

$$p'(t) = p(t) - \frac{1}{T} \left(\sum_{t=0}^{T} p(t) \Delta t \right) \tag{3.1}$$

Where p' is the fluctuating pressure signal, p is the instantaneous pressure signal, T is the total sampling time and Δt is the sample time. Next a fast Fourier transform (FFT) is performed in order to convert the pressure signal to the frequency domain:

$$\hat{p}(f) = \frac{1}{\sqrt{T}} \int_0^T p'(t) e^{-2\pi i f t} dt \tag{3.2}$$

Here $\hat{p}$ is the pressure as a function of discrete frequencies (f) and $i = \sqrt{-1}$. Due to the Nyquist theorem [35] the frequency bandwidth will be half the sampling frequency ($100kHz/2 = 50kHz$). Hamming windowing was applied to help reduce the noise [36]. The power spectral density of the fluctuating pressure signal is now described by:

$$\Phi_{pp}(f) = \hat{p} \cdot \hat{p}^* \tag{3.3}$$

Where Φ_{pp} is the PSD of the fluctuating pressure signal and $\hat{p}^*$ is the complex conjugate of $\hat{p}$. The root mean square of the fluctuating pressure (p_{rms}) can now be calculated as follows:

$$p_{rms} = \sqrt{\int_{-\infty}^{\infty} \Phi_{pp}(f) df}. \tag{3.4}$$

Another way to characterize a disturbance source is with the expected peak value in he time domain for a certain frequency range. This can be done by using the 3σ value which can be determined from a PSD as follows:

$$3\sigma[f_1 - f_2] = 3\sqrt{\Delta f \cdot \sum_{f=f_1}^{f_2} \Phi_{pp}(f)}, \tag{3.5}$$

where σ is the standard deviation. The 3σ value is the maximum expected value for which it is 99.73% probable breaks will not occur at or above this value.

3.2.1 Scaling

In order to make comparisons of pressure fluctuations in the frequency spectrum for different geometries or flow speeds, the frequency spectrum can be made non-dimensional. The non-dimensional frequency can be described by using the Strouhal number St:

$$St = \frac{f \cdot L}{U} = \frac{f \cdot d_o}{u_o}. \tag{3.6}$$

Here f is the frequency and L and U are suitable length scales and velocity scales respectively. For the velocity scale it can be chosen to use the bulk velocity u_b or the orifice velocity u_o which can be defined by using conservation of mass:

$$u_o = \frac{u_b \cdot D^2}{d_o^2},$$

(3.7)

where D is the pipe diameter. The length scale should be chosen in such a way that the pressure fluctuations in the frequency spectrum collapse. In order to find a universal scaling law which represents different sorts of noise generating geometries such as pipe bends and sudden expansions or contractions, choosing the length scale is important. Even though other geometries than single hole orifices are outside the scope of this research, the length scale should still be chosen well. However, choosing the length scale is not trivial. It can be chosen as the orifice diameter d_o [37, 25], the difference between the pipe diameter and orifice diameter $(D - d_o)$ [38, 26], or as the thickness of the orifice plate t_o [39, 40]. In the current research it is chosen to use the orifice diameter (d_o) as the length scale and the orifice velocity (u_o) as the velocity scale, as shown in Equation 3.6

Normalizing the RMS value can be done by using a universal scaling factor [41]:

$$p_{rms}^* = \frac{p_{rms}}{\rho u_o^2} \frac{D}{d_o},$$

(3.8)

where p_{rms}^* is the normalized RMS value. Knowing that $p_{rms}^* \propto (\rho u_o^2)(d_o/D)$ comparing this to Equation 3.4 it can be found that $\Phi_{pp} \propto (\rho u_o^2)^2 (d_o/D)^2$. In order to normalize the frequency term of Φ_{pp} it is multiplied by (u_o/d_o), similar to the way frequency can be normalized to the Strouhal number. The resulting normalized PSD can be described by:

$$\Phi_{pp}^* = \frac{\Phi_{pp}(f)}{(\rho u_o^2)^2} \left(\frac{D}{d_o}\right)^2 \frac{u_o}{d_o}.$$

(3.9)

However, using this normalization method does not take into account the orifice thickness, t_o. In order to understand the influence of orifice geometry including orifice thickness on pressure fluctuations, the PSD can be scaled by the pressure drop itself. Normalizing by the pressure drop gives information on the amount of pressure fluctuations generated per pressure drop. This information can be useful when designing the most optimal orifice for a given pressure drop. Scaling by pressure drop can be done as follows:

$$\Phi_{pp,\Delta p}^* = \frac{\Phi_{pp}(f)}{\Delta p^2} \frac{u_o}{d_o}.$$

(3.10)

It should be noted that in order to use this scaling method, the pressure drop needs to be measured or determined by simulation if an analytical solution is not available.

Chapter 4

Numerical approach

In order to predict behaviour of orifices in real life, large eddy simulations are performed and numerical analysis is done. In this chapter it is explained how the simulations are setup, including the meshing, boundary conditions and initial conditions. Additionally the data extraction and analysis of data from the simulations is explained.

4.1   Simulation setup

Simulations are performed using commercially available Computational Fluid Dynamics (CFD) based software Simcenter STAR-CCM+, developed by Siemens Digital Industries Software. The computational domain contains a long pipe upstream of the orifice, an orifice and an outlet pipe. The inlet and outlet pipes are both of length $20D$ and the orifice is specified as thickness t_o and diameter d_o. A schematic overview of the computational domain can be seen in Figure 4.1. Simulations were carried out for thick orifices of porosities $\beta = 20\%$ and 31% and thickness ratio's of $t_o/d_o = 2$ and 4. The simulations were based on simulations done by Kottapalli, which were done for thin orifices of $\beta = 20\%$ and 31% and $t_o/d_o = 0.5$ [34]. Comparisons in the results section will be including both results from the thin and thick orifice simulations. The origin of the simulations was chosen at the outlet of the orifice for easy comparison with experiments.
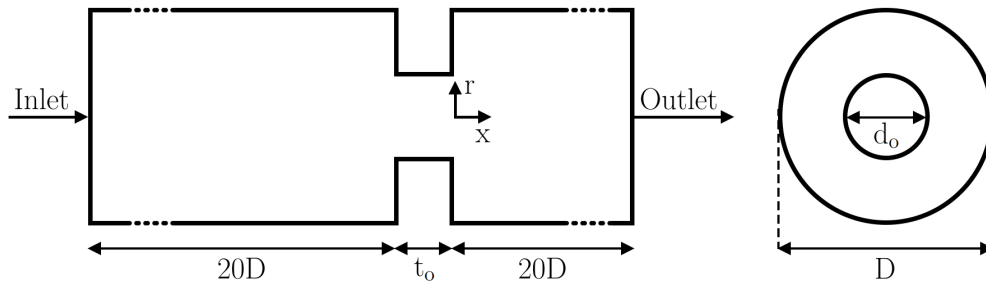
Figure 4.1: Schematic overview of the side view (*left*) and cross section (*right*) of the computational domain used in LES

For the LES it is important that the flow can become fully developed before it reaches the region of interest, in this case the orifice. A fully developed state means that the statistics of the flow properties remain constant over the domain. For this reason a long inlet pipe is used. The flow at the outlet should also be developed again in a way that no flow interaction with the outlet influences the behaviour near the orifice.

4.1.1 Meshing

Meshing is an important part of fluid simulations. In order to have reliable results from the LES, the mesh should be sufficiently refined. However, as the amount of cells in the domain increase, the simulation time also increases. It is therefor important to find a good balance between having enough cells and keeping the simulation time.

For the meshing of the domain a polyhedral mesher is used together with a prism layer mesher and a surface remesher for any automated mesh refinement that needs to be done. The polyhedral mesher is used for the bulk of the domain because it is a general purpose, reliable and robust mesher [42]. The mesh size is based on the Taylor microscale extracted from Reynolds-averaged Navier-Stokes simulations. The Taylor microscale is evaluated at the axial centerline and the mesh base size is chosen to be smaller than the Taylor microscale. A plot for the Taylor microscale can be found in Appendix B. It should be noted that the cell sizes in STAR-CCM+ are defined as a function of the cell volume (V_c):

$$Cellsize \approx 1.2 \cdot V_c^{\frac{1}{3}} \tag{4.1}$$

A base size of 0.45mm is used for the bulk of the domain and the prism layer mesher ensures that the transition of the meshsize from the wall to the inside of the mesh is smooth. Within STAR-CCM+ the quality of the mesh can be checked using a mesh diagnostics report. The mesh diagnostics checks the quality of the cells and the quality of the relation between neighbouring cells. The meshsize in the region of the orifice and downstream of the orifice is reduced to 20% of the meshsize in the rest of the domain, because the highest pressure fluctuations and vortex structures are expected to appear in this region. Local mesh refinement near the orifice ensures that the flow phenomena in that region is captured correctly. Determining the mesh size from the wall inward is done by looking at the dimensionless wall distance y^+. The dimensionless wall distance is defined in the following way:

$$y^+ = \frac{u_\tau y}{\nu} \tag{4.2}$$

Where y is the distance from the wall and ν is the kinematic viscosity of the fluid and u_τ is the wall friction velocity given by;

$$u_\tau = \sqrt{\frac{\tau}{\rho}} \tag{4.3}$$

Where τ is the shear stress and ρ the fluid density. The first wall cell is kept to $y^+ \approx 1$ near the orifice and for the rest of the domain $y^+ << 1$. Figure 4.2 shows a cut out section of the mesh including the orifice of $\beta = 20\%$ and $t_o/d_o = 2$.
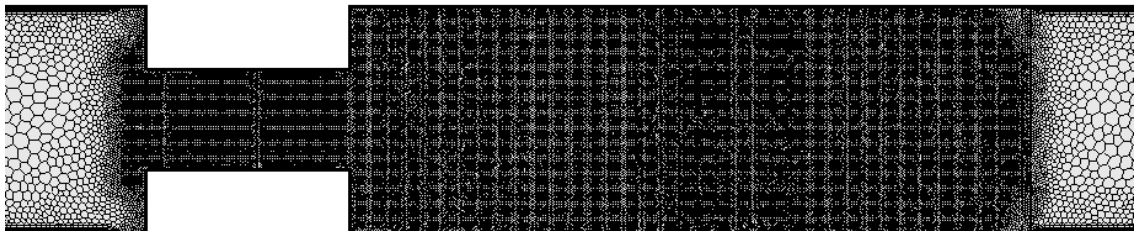
Figure 4.2: Cut out section of the cross-sectional view of the mesh used in the LES for the case of $\beta = 20\%$ and $t_o/d_o = 2$

The total cell count is approximately 8 million cells for each of the simulations, depending on the porosity and thickness to diameter ratio of the orifice.

4.1.2 Boundary conditions

An important part of the simulation setup are the boundary conditions. The boundary conditions in a simulation have a large influence on the rate at which the flow becomes developed, the efficiency of a simulation and ultimately on the actual flow phenomena and pressure fluctuations present in the simulation. It is therefor important that the boundary conditions are chosen in a way that is physical and as efficient as possible.

Synthetic eddy method

Using the synthetic eddy method (SEM), turbulence can be generated synthetically in order to get a stabilized turbulent flow faster. A mean flow is defined and spatially and temporally correlated unsteady fluctuations are generated and superimposed on this flow at the inlet pipe [43]. The inlet pipe must be long enough to allow for the flow to develop before it reaches the region of interest.

Applying the SEM in STAR-CCM+ is done by setting the turbulent length scale and the turbulence intensity (TI). The turbulent length scale must span at least two cells to produce correlated signals ($l_t > 2\Delta$). However, for low mach numbers, as considered in this study, the turbulent length scale can be defined as $l_t = D/2$ [44], which is larger than the previously mentioned minimum length scale. The TI is defined as:

$$I = \frac{u_{rms}}{\bar{u}}, \tag{4.4}$$

where I is the turbulence intensity, u_{rms} is the RMS value of the velocity and $\bar{u}$ is the mean velocity. The TI is set at $I = 5\%$, determined by previously done simulations. If the TI is chosen too low, the flow will go laminar and if the TI is set too high the flow becomes very unstable and non-physical.

Recycling plane method

In order to have a constant influx of turbulent developed flow towards the region of interest, the recycling plane method is used. If a periodic boundary condition was used connecting the outlet of the fluid domain to the inlet of the fluid domain, the effects of the orifice would influence the next flow-through. Essentially, the results would correspond to that of a domain with multiple orifices in series. Solving this would require having a very long inlet and outlet to let the flow settle again before reentering the orifice. A different solution is to use the recycling plane method, where the inlet pipe has periodic boundary conditions and the flow from the inlet pipe are mapped onto the region of interest. This way there is a constant supply of developed turbulent flow to the orifice. The periodic boundary condition of the inlet pipe is set to a constant mass flow rate defined as:

$$\dot{m} = \rho A_p u_b \tag{4.5}$$

Where $\dot{m}$ is the mass flow rate. The mass flow rate is set to 0.076 kg/s which corresponds to a bulk velocity of 1.2 m/s. A schematic overview of the recycling plane method can be seen in Figure 4.3.

Pressure outlet

The outlet boundary condition of the computational domain is set to a pressure outlet of a gauge pressure of 0 Pa. This outlet does not influence the pressure drop from inlet to outlet and all pressure fluctuations at the outlet are forced to zero.
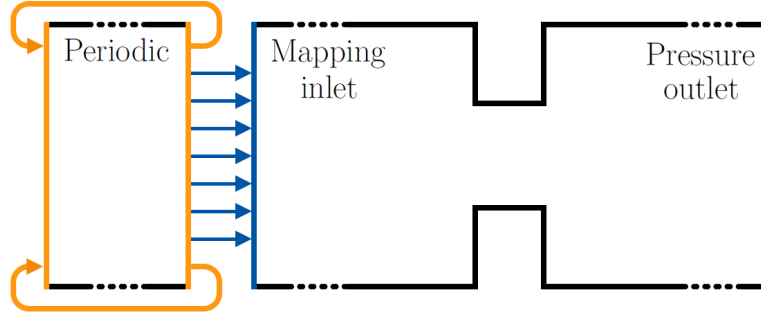
Figure 4.3: Schematic overview of the boundary conditions used in LES

4.1.3 Models and solvers

Time stepping

Having the correct temporal resolution is important for the accuracy of the results from the LES. Because an explicitly discreticed flow solver is used, the Courant-Friedrichs-Lewy (CFL) condition or Courant number should be considered [45]. The CFL conditions says that any travelling length of information during one timestep should be smaller than the distance travelled between two cell centeriods. In order to have a correct solution from the simulation the Courant number should be kept below $CFL < 1$ for all cells. The CFL number at a given location is described by:

$$CFL = \frac{u_i \Delta t}{\Delta x_i}, \tag{4.6}$$

where u_i is the velocity magnitude in the cell, Δt is the time step and Δx the distance between the mesh elements. The criterion of $CFL < 1$ is satisfied for the thick orifice simulation at a time step of $\Delta t = 2 \cdot 10^{-6}$ s. For most of the cells $CFL < 0.2$ which helps ensure a good solution. The time step also determines the high end of the frequency range that can be extracted from the simulation. The maximum frequency that can be extracted from the simulation with this time step is $2.5 \cdot 10^5$ Hz, which is more than sufficient because the main focus of this study is on low frequency behaviour of frequencies below 1000 Hz. The lower boundary of the frequency spectrum is determined by the length of the simulated physical time. Using this time step and mesh as explained in Section 4.1.1, the simulations were carried out on a cluster of ASML. For each of the simulations 80 cores were used resulting in a computing time of approximately 4 days per 0.1 second of simulated physical flow.

SGS modelling

Within the LES, subgrid scale modelling is used to model the smallest length scales instead of solving the Navier-Stokes equations for these small structures. In this way a lot of computational cost is saved. In STAR-CCM+ the wall adapting local eddy-viscosity (WALE) model is used as the SGS model [46, 47]. The WALE model calculates the subgrid scale turbulent eddy viscosity ν_t, which is needed to model the SGS stress tensor. The subgrid scale turbulent eddy viscosity is defined as:

$$\nu_t = C_w^2 \Delta x^2 S_w, \tag{4.7}$$

where C_w is a model dependent constant with a default value of $C_w = 0.5$ and S_w is the deformation parameter defined as:

$$S_w = \frac{(S_{ij}^d S_{ij}^d)^3 / 2}{(S_{ij}^d S_{ij}^d)^{5/4} + (S_{ij} S_{ij})^{5/2}}, \tag{4.8}$$

where S_{ij}^d is defined as:

$$S_{ij}^d = \frac{1}{2}\left[\left(\frac{\partial \bar{u}_i}{\partial \bar{x}_j}\right)^2 + \left(\frac{\partial \bar{u}_j}{\partial \bar{x}_i}\right)^2\right] - \frac{1}{3}\delta_{ij}\left(\frac{\partial \bar{u}_k}{\partial \bar{x}_k}\right). \tag{4.9}$$

Here δ_{ij} is the Kronecker delta, which is 0 if $i \neq j$ and 1 if $i = j$. Substituting into the filtered Navier-Stokes equations the following relation is found which includes a term to represent the turbulent eddy viscosity:

$$\frac{\partial u_i}{\partial t} + u_j \frac{\partial u_i}{\partial x_j} = -\frac{1}{\rho}\frac{\partial p}{\partial x_i} + \frac{\partial}{\partial x_j}\left[(\nu + \nu_t)\left(\frac{\partial u_i}{\partial x_j} + \frac{\partial u_j}{\partial x_i}\right)\right] + \frac{F_i}{\rho}. \tag{4.10}$$

Discretization

Discretizing the convection terms of the Navier-Stokes equations is done using the Bounded Central-Differencing (BCD) scheme. The BCD scheme is a combination of a pure central-differencing scheme, a blend of central differencing and second order upwind scheme and a first order upwinding scheme. The first order upwinding scheme is only used when the convection-boundedness criterion (CBC) is satisfied, which helps to reduce the computational effort [48]. Temporal discretization is done using a 2nd order time step scheme.

4.2 Data extraction

In this section the extraction of pressure and force data is explained. In general all data is extracted after about three flow-through cycles, which corresponds to 0.1s of simulated time. This is done to account for any initial errors and only includes data when the flow has been stabilized.

4.2.1 Pressure

Extracting the pressure signal from the simulation at a given location can be done using a point probe and monitoring the pressure at that probe over multiple time steps. The pressure signal can then be processed in a similar fashion as described in Section 3.2 in order to determine the corresponding pressure PSD at that location. However, in order to compare the pressure signal from the simulation to measurements done, the area of the pressure transducer probe has to be taken into account. In the study by Lueptow [49] it was found that the measured wall pressures are influenced by the surface area of the pressure transducers. It was concluded that for normalized diameter of the transducer surface of $d^+ > 19$ the PSD and RMS of the wall pressures are underestimated. The normalized diameter of the transducer surface is defined as;

$$d^+ = \frac{u_\tau d_s}{\nu} \tag{4.11}$$

Where d_s is the pressure transducer surface diameter. It was found that for the transducers used in this study, the normalized diameter was $d^+ \approx 150$. One approach would be to use a correction factor for the measured wall pressures as proposed by Corcos [50] or Willmarth and Roos [51]. Calculating the required correction factors is complex and therefor it is chosen to use a different approach. Instead of correcting the measured signal, extracting the pressure from the simulation is done by monitoring the surface average of the pressure over a circular section on the wall corresponding to the pressure transducer size. The surface averaged pressure signal can then be processed and compared to measurements. The averaging of the pressure signal occurs because of eddies that are smaller than the size of the probe area. The eddies cause localized pressure fluctuations and as these fluctuations are situated in a space smaller than the pressure transducer, the transducer only registers the average effect. The frequency at which the averaging behaviour will appear for a circular deflection censor is described by Lueptow [49] as:

$$f_0 = \frac{7.7 \cdot u_c}{2\pi \cdot d_s} \tag{4.12}$$

Where f_0 is the first frequency at which averaging will occur and u_c is the convection velocity. Because the near field pressure sensors are located in a turbulent environment, it is difficult to extract the convection velocity. Approximating the convection velocity by using the bulk velocity instead $f_0 \approx 600$ Hz is found.

4.2.2 Force

In order to model far field pressure fluctuations an acoustic force source term acting on a body in the near field has to be extracted from the simulations. This is done within STAR-CCM+ by defining a field function. The force source term is extracted by taking a volume integral of all the forces acting in axial direction over a volume which includes the orifice. The relevance of the chosen control volume will be discussed in Section 5.2.3. The force term is based on the acoustic power as described by Rienstra and Hirschberg [52] as follows:

$$\mathbf{P} = -\iiint_V \left[\rho_0 \mathbf{u_0} \cdot (\omega' \times \mathbf{u'}) + \rho' \mathbf{u'} \cdot (\omega_0 \times \mathbf{u_0}) \right] d\mathbf{x}. \tag{4.13}$$

Here $\mathbf{P}$ is the acoustic power, ω' is the fluctuating vorticity vector and $\mathbf{u'}$ is the fluctuating velocity vector. The variables subscripted with 0 are the mean values of those variables. It is assumed that the flow is incompressible, which removes the second term of the equation. Upon removing the mean velocity dot product the equation for the acoustic force is found:

$$\boldsymbol{f} = -\iiint_V \rho \left(\boldsymbol{\omega'} \times \boldsymbol{u'} \right) dV \tag{4.14}$$

Where $\boldsymbol{f}$ is the acoustic force vector. Using this equation, the force generated over an arbitrary volume can be logged over time to get a force signal. The axial component of this force signal is later used in modelling the far field pressure fluctuations.

4.3 Data Analysis

The analysis of the data extracted from the simulations is mostly done using the numerical computing software MATLAB. For calculating the far field pressure fluctuations the PlaNet3D is used, which is a MATLAB tool developed in house at ASML [53]. PlaNet3D uses lumped mass dynamic modeling and can be used to model the effects of mass, elasticity and damping in a network of ducts and attached components. It is assumed that pressure waves in a network can be described by the one-dimensional acoustic wave equation:

$$\frac{1}{c^2} \frac{\partial^2 p'}{\partial t^2} - \frac{\partial^2 p'}{\partial x^2} = \frac{\partial F'}{\partial x}, \tag{4.15}$$

where c is the speed of sound. Because mass and momentum conservation equations are analogous with those of a mass-spring system, a network of ducts can be described by a system of lumped mass-spring systems. An example of a lumped mass-spring system as used in PlaNet3D can be seen in Figure 4.4:

The governing equation of a mass-spring system can be described by:

$$m\ddot{x} + (C_1 + C_2)x = F_{w \to f} \tag{4.16}$$

Where m is the mass of the fluid in the duct, x the distance and $F_{w \to f}$ the force acting from the wall to the fluid. The stiffnesses C_1 and C_2 are inversely proportional to the duct length (KA_p/L). Where K is the fluid bulk modulus and A_p is the cross sectional pipe area. It should be noted that the PlaNet3D model is only used to predict pressure fluctuations that are a result
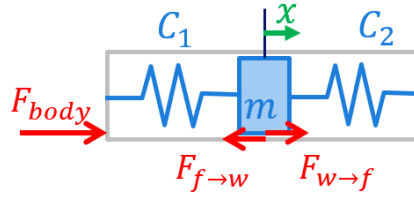
Figure 4.4: A free body diagram of a lumped mass-spring element as used in PlaNet3D for modeling acoustic pressure waves

of acoustic forces, the hydrodynamic component is not taken into account. A visualisation of the network using PlaNet3D can be seen in Figure 4.5. This figure displays the hard ducted section (thick line) connected to the PU tubes (thin lines). The PU tubes continue further outside of the frame with a total length of 10m each.
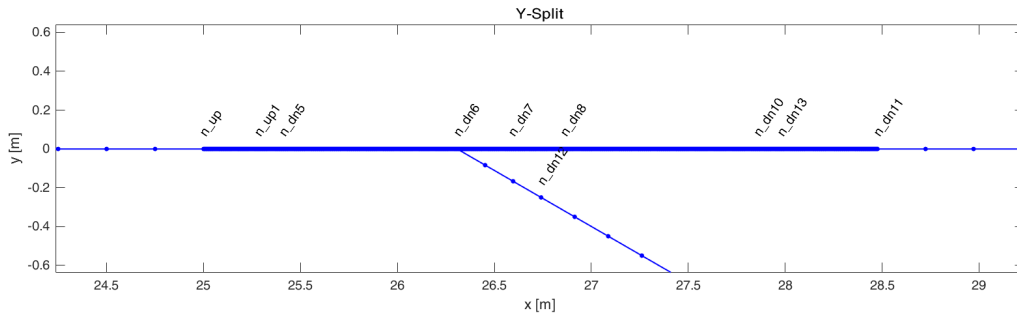
Figure 4.5: Schematic overview of the network of lumped mass-spring systems using PlaNet3D

Within the PlaNet3D model multiple nodes are defined between which connections are made to create a network which represents the real life test setup. The nodes are placed to represent the geometric properties of the test setup such as the inlet and of the hard-ducted test section, the PU tubing and the pressure transducer locations. The acoustic force term used to predict far field pressure fluctuations is extracted from the STAR-CCM+ simulation as explained in Section 4.2.2. The acoustic force PSD is used as an input and is converted to a duct pressure. The PlaNet3D toolbox is then used to determine a transfer function between the input duct and the nodes which represent the pressure transducers. The relation between the duct PSD and transducer PSD is described by:

$$PSD_n(f) = |H_{d \to n}(f)|^2 \cdot PSD_d(f) \tag{4.17}$$

Where PSD_n is the PSD at the node of interest, $H_{d \to n}$ is the transfer function from the duct to the node and PSD_d is the PSD at the input duct.

Chapter 5

Results

In this chapter the results from the measurements and simulations will be compared. First a comparison will be made between pressure fluctuation measurements for orifices of different geometries. Next, results from the simulations will be compared to each other and lastly the experimental data will be compared to the data extracted from the simulations.

5.1   Experimental results

By comparing measurement results using different configurations, the effect of that change can be quantified. The near field pressure fluctuations will be discussed first as well as the far field pressure fluctuations. Comparing PSDs from a single measurement at several locations can help understand where the maximum pressure fluctuations are located and how the pressure fluctuations propagate through the system. Then, comparing PSDs from measurements of orifices with varying porosity and thickness to diameter ratio, the influence of the geometry can be determined.

All pressure measurements were carried out at a bulk velocity of $u_b = 1.2$ m/s which corresponds with a bulk Reynolds number of $Re_b \approx 12000$, unless specified differently. At this bulk velocity the flow is turbulent but non-cavitating. This bulk velocity was used because it was nearing the high end of the pumps capacity and both the pressure loss (Δp) and the root mean square of the pressure fluctuations (p'_{rms}) scale with the square of the mean flow velocity [10]. Using a high velocity therefor gives a better signal which can easily be differentiated from noise. In the pressure PSDs peaks were found at frequency multiples of 50Hz. These peaks are due to the net power frequency and were filtered out.

Several experiments were carried out comparing thin and thick orifices with porosities of $\beta = 20\%$ and $\beta = 31\%$ (orifice diameters of $d_o = 4$ and 5mm). The comparison of near field and far field pressure PSDs for each of these cases can be found in Appendix C. According to Idelchik [3] the pressure drop induced by thick orifices does not change significantly when the orifice qualifies as thick ($t_o/d_o > 1.5$). It is found that pressure fluctuations are proportional to the pressure drop [10], so the pressure fluctuations for thick orifices of different thicknesses is expected to be the same. A comparison between near field and far field pressure fluctuations for thick orifices of $t_o/d_o = 2$ and 4, and porosities $\beta = 20\%$ and 31% can be found in Appendix D. It was found that the pressure fluctuations for these cases were indeed nearly identical. To improve visibility, measured pressure PSDs of thickness to diameter ratio $t_o/d_o = 4$ are excluded in some of the figures.

5.1.1 Near field pressure

The near field pressure measurements take place at $x/D = 1, 2, 3$ and 6 downstream of the orifice and are within the region where the vortex structures are generated and dissipated. Therefor, near field pressure fluctuation measurements cannot be used to directly calculate the pressure waves that will travel through the water ducts towards other regions of the system. However, comparing near field pressure fluctuation measurements to simulations is straightforward, as the positions of the pressure transducers are within the simulated domain. Near field pressure measurements can therefor be used to validate simulations. Measurements in the near field can also be used to compare the effects of different orifice properties such as thickness and porosity, or making comparisons with data from other studies.

Before comparing the influence of different geometries to each other, the pressure fluctuations at the different near field positions are discussed. Figure 5.1 displays the near field pressure PSDs for thin and thick orifices of $\beta = 20\%$ and 31% ($d_o = 4$ and 5mm).

(a) Thin: $\beta = 20\%$, $t_o/d_o = 0.5$

(b) Thick: $\beta = 20\%$, $t_o/d_o = 2$

(c) Thin: $\beta = 31\%$, $t_o/d_o = 0.5$

(d) Thick: $\beta = 31\%$, $t_o/d_o = 2$
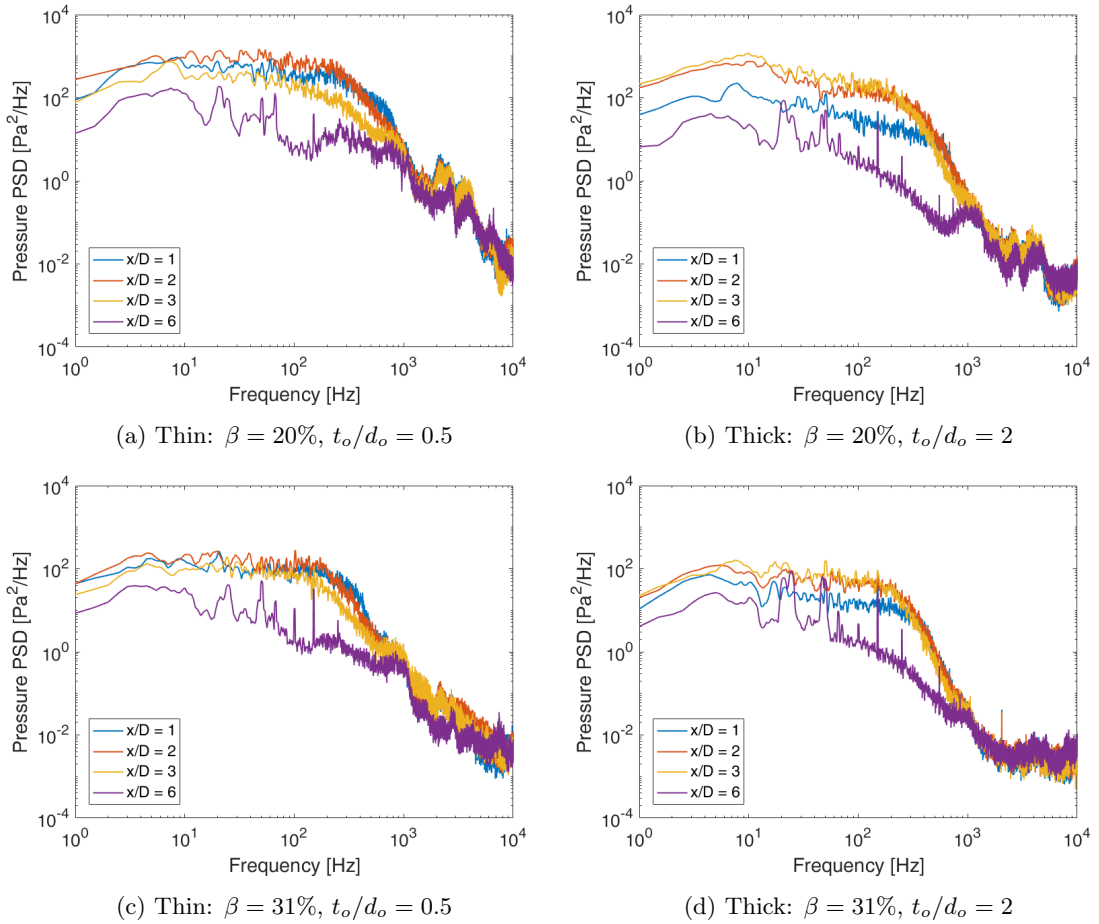
Figure 5.1: Near field pressure PSDs of thin and thick orifices, $Re_b \approx 12000$

Looking at these PSDs it becomes clear that the position of maximum pressure fluctuations are located differently for the thin and the thick orifices. The thin orifices show the largest pressure fluctuations at positions $x/D = 1$ and 2, whereas the thick ones show maximum pressure fluctuations at positions $x/D = 2$ and 3. This is in agreement with Qing et al. [25] who found the maximum pressure fluctuations at $x/D = 1.7$ for thin orifices. Both thin and thick orifices show that at a distance of $6D$ the pressure fluctuations have started decaying significantly.

Influence of orifice geometry on near field pressure fluctuations

Evaluating the influence of orifice geometry on near field pressure fluctuations is done by comparing the PSDs at several near field locations. Figure 5.2 shows the PSDs for thin and thick orifices of $\beta = 20\%$ and 31%.

(a) x/D = 1

(b) x/D = 2

(c) x/D = 3

(d) x/D = 6
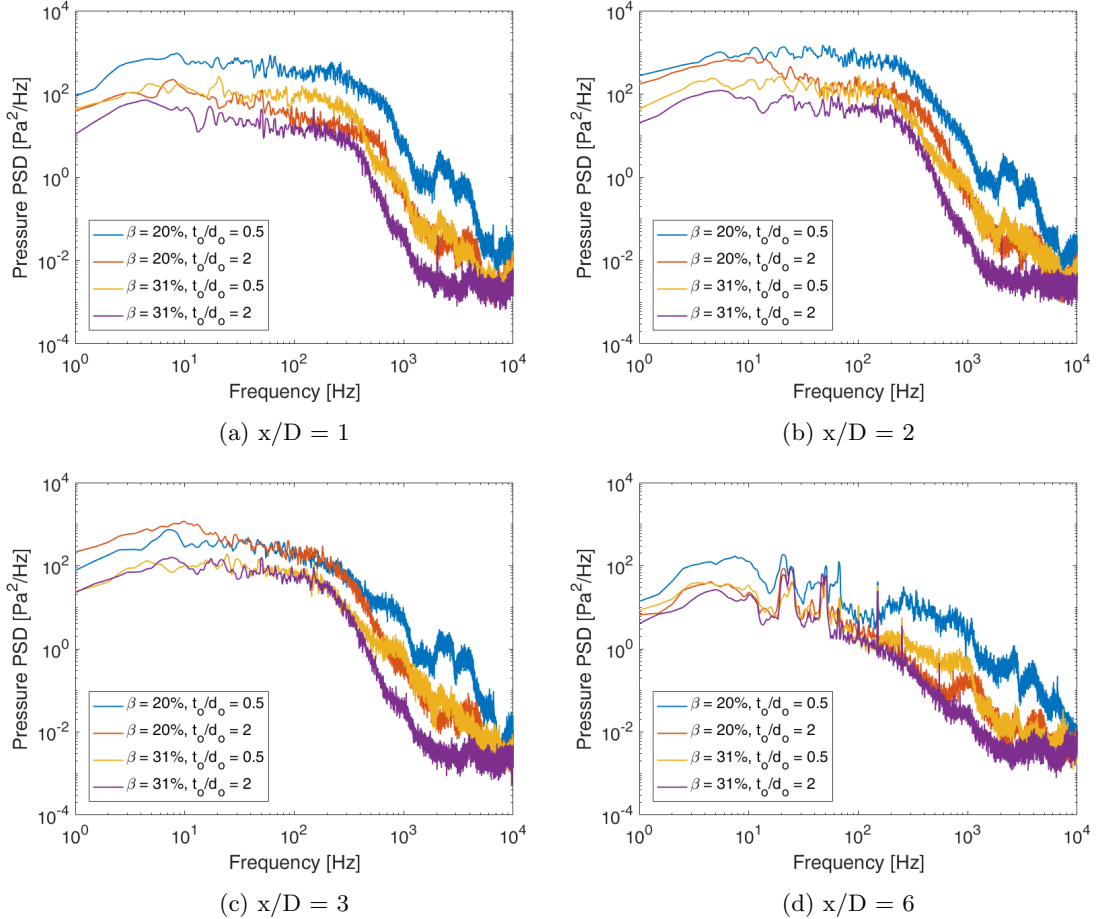
Figure 5.2: Near field comparison of pressure PSDs for thin and thick orifices of $\beta = 20\%$ and 31% ($d_o = 4$ and 5mm), $Re_b \approx 12000$

It is evident that for each of the porosities at each of the positions the thin orifice has an overall higher PSD than the thick orifice, which is as expected. It can also be seen that for orifices of the same thickness to diameter ratio and different porosities the larger porosity orifices generate a generally lower PSD. This again corresponds to the expectations, as for a more restrictive orifice the generated pressure fluctuations are anticipated to be higher. It should be noted that the bulk velocities for each of the measurements above is the same and the pressure drop for each of these cases is different. By scaling the pressure PSDs with the pressure drop squared, it can be found what the noise contribution per unit pressure drop is. In order to perform this scaling a measured or simulated pressure drop is required. The pressure drops acquired from measurements can be found in Table 5.1.

Table 5.1: Measured pressure drops for orifices of several geometries

Porosity β	Thickness ratio t_o/d_o	Pressure drop Δp [Pa]
20%	0.5	23300
20%	2	16540
31%	0.5	8070
31%	2	7570

A large difference in pressure drop for the thin and thick orifices of 20% is observed. For the 31% case the pressure drop difference between thin and thick is much less significant. The measured near field pressure PSDs scaled with the pressure drop squared can be found in Figure 5.3.

(a) x/D = 1   (b) x/D = 2   (c) x/D = 3
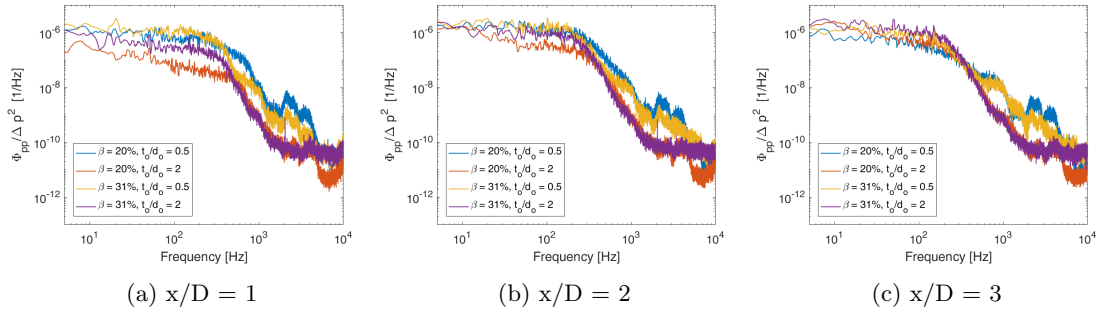
Figure 5.3: Near field comparison of pressure PSDs scaled with pressure drop for thin and thick orifices of $\beta = 20\%$ and 31% ($d_o = 4$ and 5mm)

It can be seen that generally the thin orifices generate larger pressure fluctuations than the thick ones. Also, for the thick orifices the 31% case generally produces more pressure fluctuations than the 20% case.

5.1.2 Far field pressure

Conducting far field pressure measurements gives a better understanding of the influence of orifices on pressure fluctuations traveling through a system. First, the contribution of hydrodynamic and acoustic forces on the pressure fluctuations will discussed. Then the measurements with different orifices will be compared, examining the influence of the orifice geometry on pressure fluctuations.

In line and Y-splitter setup

In order to understand the contribution of the hydrodynamic and acoustic forces, two setups are compared. One setup with straight ducting and flow at the far field, referred to as "in line" setup and one setup with a side branch and no flow at the far field pressure measurements, referred to as "Y-splitter" setup. A schematic overview of the Y-splitter setup with no flow at the far field is given in Figure 3.1 and the schematic overview of the in line setup with flow can be found in Figure 5.4.

Figure 5.4: Schematic overview of the in line test setup

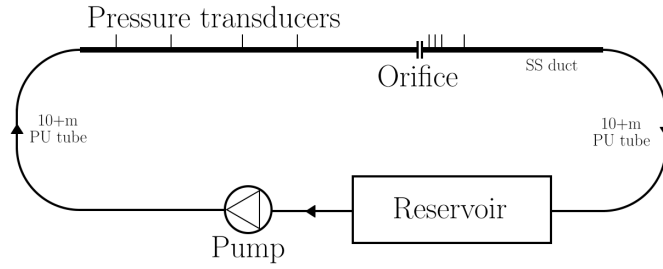The far field pressure measurements are also compared to experiments where there is no flow. The no flow experiments are used to determine the noise present in the system. Pressure measurements are taken and post processed to be visualized in PSD form as described in Section 3.2. A comparison between the pressure PSDs measured using the in line and Y-splitter setups can be seen in Figure 5.5.

(a) Thin orifice comparison ($t_o/d_o = 0.5$)

(b) Thick orifice comparison ($t_o/d_o = 2$)
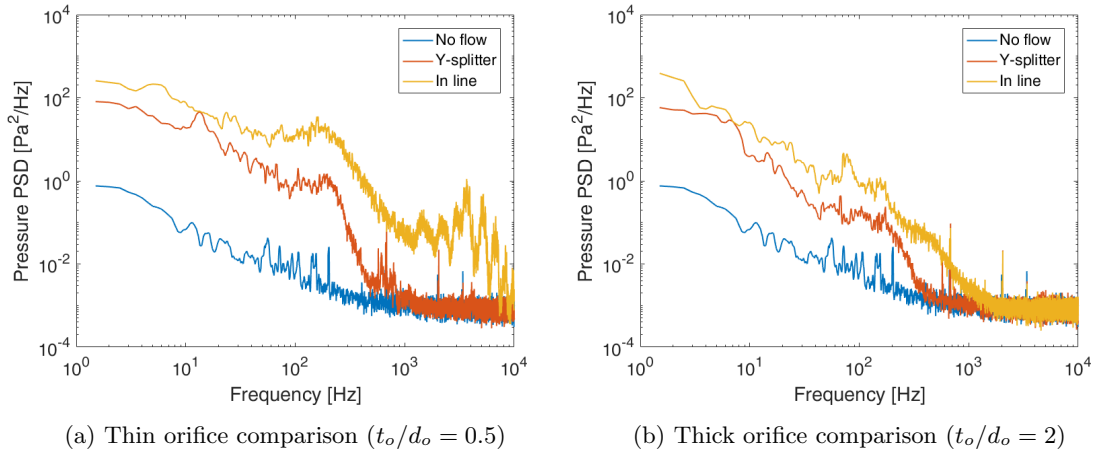
Figure 5.5: Comparison of the measured far field pressure PSD for the in line and Y-splitter setup for thin and thick orifices of $\beta = 20\%$, both at a distance of 238D upstream of the orifice, $Re_b \approx 12000$

It is evident that the in line setup shows generally higher PSD values over the whole frequency bandwidth than the Y-splitter setup for the thin as well as the thick orifice. The reason for this is that the flow component is not present within the Y-splitter setup. The near field pressure fluctuations were measured as well for both setups. No significant difference was found between the two. A comparison between the two setups and the influence on the near field pressure fluctuations can be found in Appendix E. It is found that the difference between the far field pressure fluctuations of the in line setup and the Y-splitter setup is due to hydrodynamic contributions of the flow past the pressure transducers. Also, because the near field pressure fluctuations are nearly identical for both cases, the noise generated by the orifice is dominant over any contributions that are made by the Y-splitter.

Influence of orifice geometry on farfield pressure fluctuations

Comparing the pressure PSDs at several far field locations gives an impression on how the pressure fluctuations propagate through the system and how they are damped. Figure 5.6 shows the pressure PSDs far field from the orifice for thin and thick orifices.

(a) Thin orifice $t_o/d_o = 0.5$ (b) Thick orifice $t_o/d_o = 2$
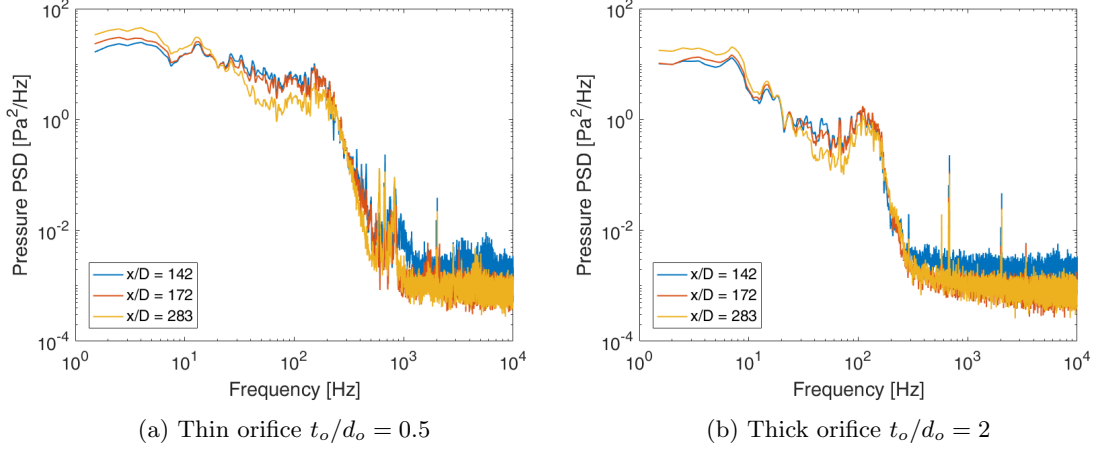
Figure 5.6: Pressure PSDs at various far field locations for orifices of porosity $\beta = 20\%$, $Re_b \approx 12000$

Comparing the pressure PSDs at several far field locations shows that the pressure fluctuations indeed are damped as they travel a farther distance. This effect is most visible in the region 10-100Hz. The far field pressure fluctuations are compared for thin and thick orifices of porosities $\beta = 20\%$ and 31%.

(a) x/D = 142   (b) x/D = 283
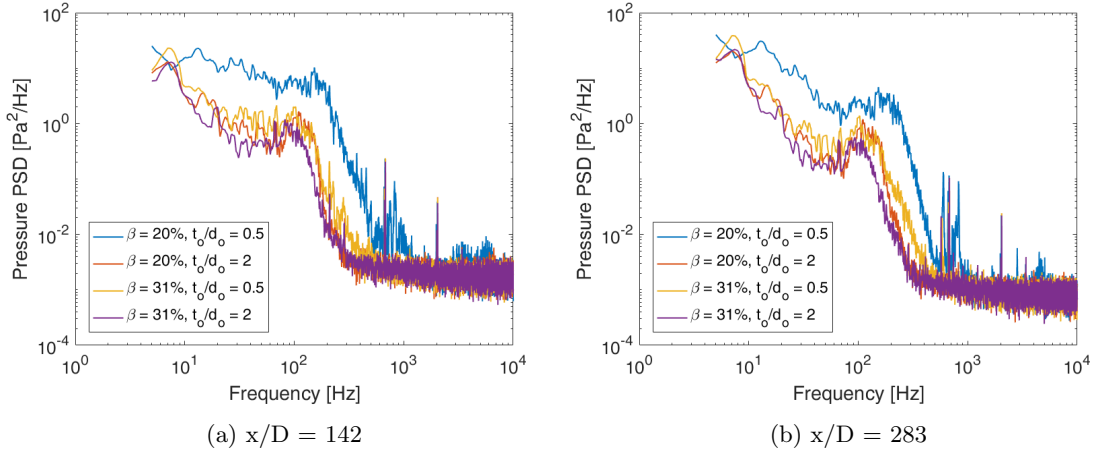
Figure 5.7: Far field comparison of pressure PSDs for thin and thick orifices of $\beta = 20\%$ and 31% ($d_o = 4$ and 5mm), $Re_b \approx 12000$

A distinct difference can be noticed between the pressure fluctuations of a thin orifice compared to a thick orifice. The PSDs of the thin orifices show larger pressure fluctuations. The thin orifice for a porosity of 20% also induce larger pressure fluctuations than that of a porosity of 31%. For the thick orifices the same behaviour is observed but the difference is much less apparent. The far field pressure PSD scaled with the measured pressure drop can be found in Figure 5.8.

(a) x/D = 142

(b) x/D = 283
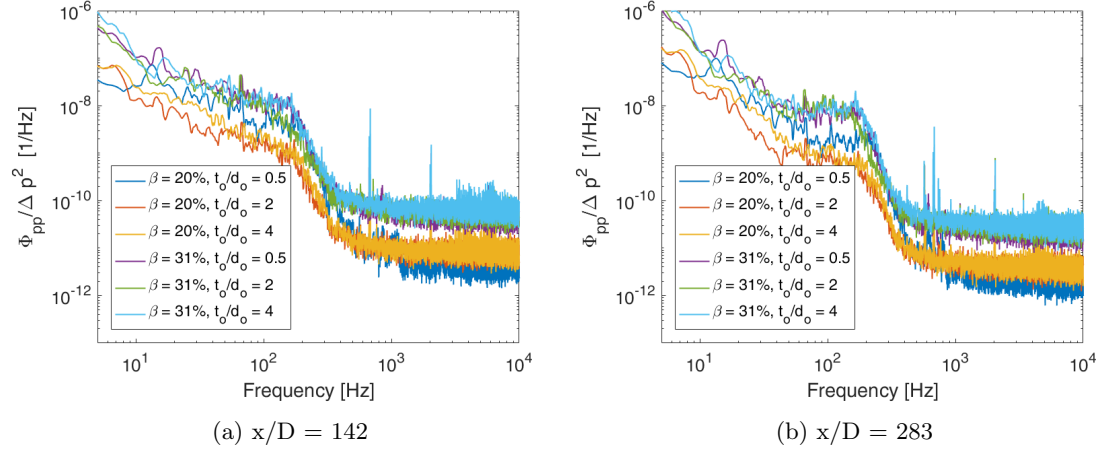
Figure 5.8: Far field pressure PSDs for thin and thick orifices from measurements, normalized using scaling with pressure drop ($Re_b \approx 12000$)

The far field scaled pressure PSDs show that 31% orifices induce more pressure fluctuations than 20% orifices. For the 20% orifices the thin one also shows generally higher pressure fluctuations than the thick ones. The difference for thin and thick orifices of $\beta = 31\%$ is less noticeable.

5.1.3 Scaling

Scaling the measured PSDs allows easy comparison of conducted measurements. It also makes it possible to model the outcome when a parameter is changed. First velocity scaling is discussed. Figure 5.9 shows the pressure PSDs at several near field locations.

(a) x/D = 1

(b) x/D = 2

(c) x/D = 3

Figure 5.9: Near field pressure PSDs for at several bulk velocities produced by an orifice of $\beta = 20\%$ (4mm) and $t_o/d_o = 0.5$

It can be seen that the PSDs behave as expected. A higher flow rate induces a larger pressure drop and larger pressure fluctuations as both Δp and p'_{rms} scale with the square of the mean flow speed. A normalized comparison using Equation 3.9 is shown in Figure 5.10.

(a) x/D = 1   (b) x/D = 2   (c) x/D = 3

Figure 5.10: Normalized near field pressure PSDs for several bulk velocities produced by an orifice of $\beta = 20\%$ $(4mm)$ and $t_o/d_o = 0.5$

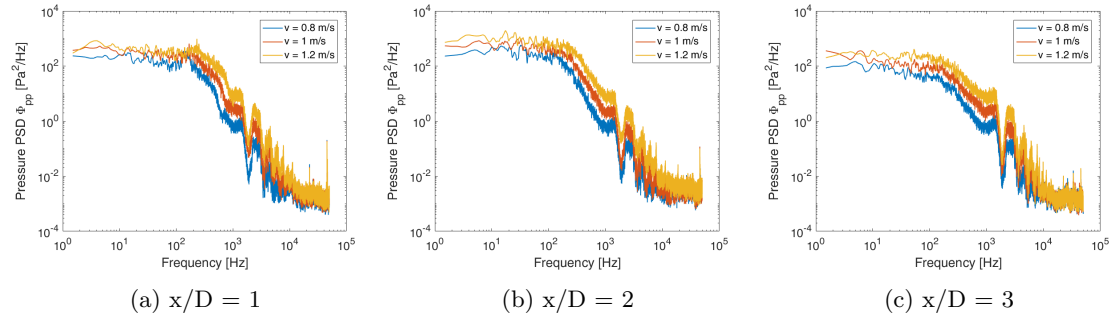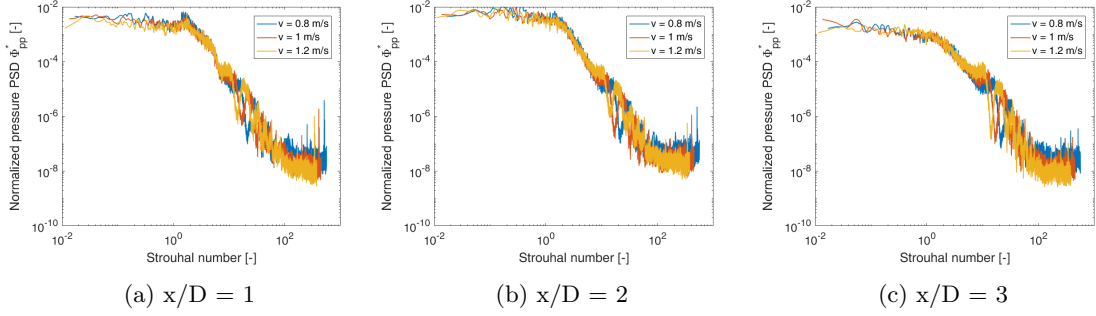The normalized PSDs show a good collapse for each of the locations, concluding that the scaling of velocity can indeed be predicted using this method. This scaling method also includes a factor for the orifice porosity. The normalized near field PSDs for thin and thick orifices are compared in Figure 5.11.

(a) x/D = 1   (b) x/D = 2   (c) x/D = 3
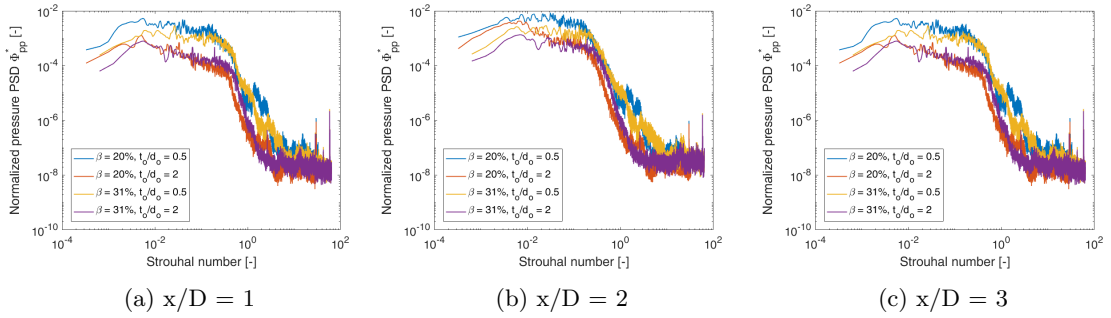
Figure 5.11: Normalized near field pressure PSDs comparing thin and thick orifices, $Re_b \approx 12000$

Using this scaling method it is found that for the 20% orifices the pressure PSD is slightly higher for the thin orifice. For the 31% case this is not apparent. It should be kept in mind that scaling using this method does not contain a factor for the thickness of the orifice.

5.2 Simulation results

In this section a look will be taken at flow fields and flow structures that are present within the fluid domain and the extracted force term. All data of thick orifices was generated for this study, the thin orifice data was taken from simulations done by Kottapalli [34] and Krabben [1].

5.2.1 Near field pressure

Multiple pressure probes were positioned on the walls of the computational domain, logging the pressure over time. The pressure PSDs of these signals were taken and the 3σ values were calculated using Equation 3.5. The 3σ value is the maximum expected pressure fluctuation with probability of 99.73%, for a given pressure spectrum. The 3σ value can be normalized by dividing it by the pressure drop extracted from the simulations. Figure 5.12 shows the 3σ values and normalized 3σ values near the orifice for orifices of several geometries.

(a) 3σ

(b) $3\sigma/\Delta p$

Figure 5.12: 3σ values as a function of position for several orifice geometries. $x/D = 0$ indicates the outlet of the orifice

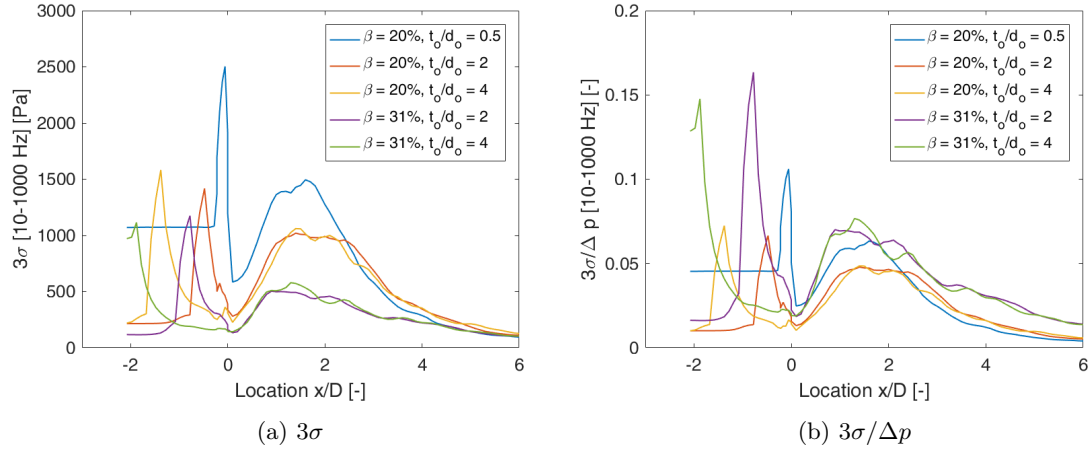Figure 5.12a shows that the maximum pressure fluctuations in the near field downstream of the orifice are largest for the thin orifice of $\beta = 20\%$. The thick orifices of equal porosity show nearly identical 3σ values. This further confirms that the thickness of an orifice no longer influences the pressure fluctuations once the orifice is qualified as thick. The locations of the peaks upstream of the orifice outlet are at the entrance of each of the orifices. The position of these peaks is different for each orifice because they each have different thicknesses. Looking at the normalized 3σ values (Figure 5.12b), it becomes clear which orifices are expected to produce the most pressure fluctuations as a function of pressure drop. It is found that the thin orifice of porosity $\beta = 20\%$ has higher 3σ values than the thick ones of the same porosity. The 31% orifices show generally larger scaled 3σ values than the 20% orifices.

Figure 5.13 shows the near field pressure PSDs extracted from LES using point probes, scaled with the pressure drop extracted from the same LES. These PSDs are extracted at the locations corresponding with the near field pressure transducers in the measurements.

(a) x/D = 1

(b) x/D = 2

(c) x/D = 3
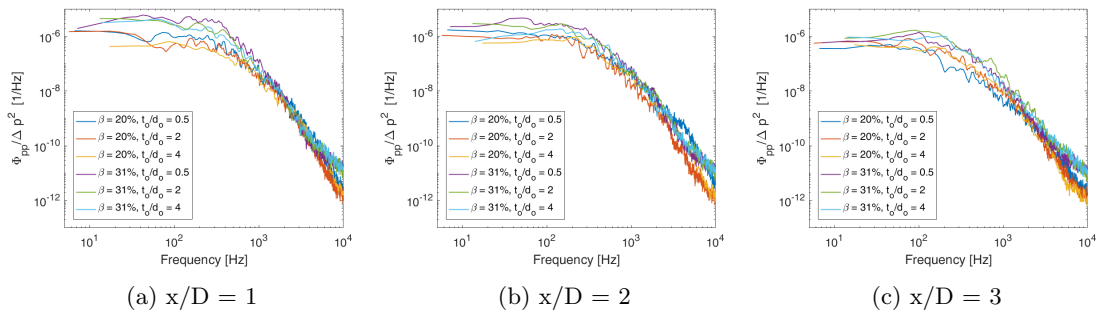
Figure 5.13: Near field pressure PSDs for thin and thick orifices extracted from LES using point probes, scaled with pressure drop ($Re_b \approx 12000$)

For the near field pressure fluctuations, orifice thickness does not show a significant difference. However, between the 20% and 31% orifices a difference in PSD is visible. It can be seen that a larger porosity leads to larger pressure fluctuations for a given pressure drop. This implies that it is better to use a smaller porosity orifice in order to induce a certain pressure drop, opposed to using multiple large porosity orifices in series.

5.2.2   Flow fields and vortex structures

Looking at the flow fields in and around an orifice gives a better understanding of what flow phenomena are responsible for the pressure fluctuations travelling through the system. Identifying flow structures like vortexes shows where the main contribution of the acoustic force comes from.

Velocity

Comparing the mean velocities of thick and thin orifices shows the difference between the two. The flow is contracted when entering the orifice.Ffor the thick orifice the flow reattaches to the wall of the orifice before expanding again. For the thin orifice the flow does not reattach. Figure 5.14 shows the mean velocity field for a thin and thick orifice of $\beta = 20\%$. Similarly, Figure 5.15 shows the mean velocity comparison for orifices of $\beta = 31\%$.

Figure 5.14: Comparison of the mean velocity for a thin and a thick orifice of $\beta = 20\%$ and an orifice thickness to diameter ratio of 0.5 and 2 respectively

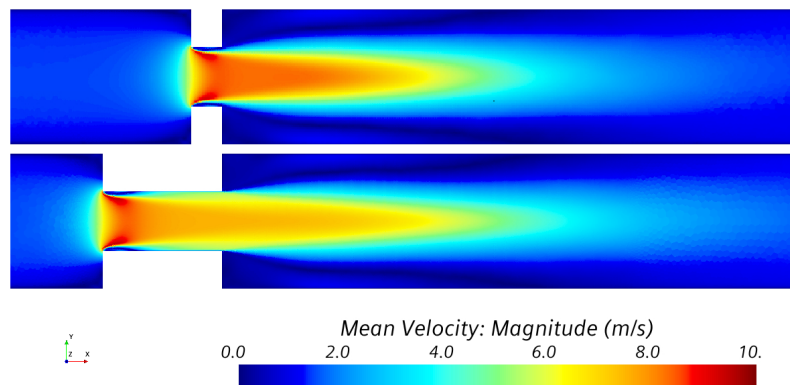Figure 5.15: Comparison of the mean velocity for a thin and a thick orifice of $\beta = 31\%$ and an orifice thickness to diameter ratio of 0.5 and 2 respectively
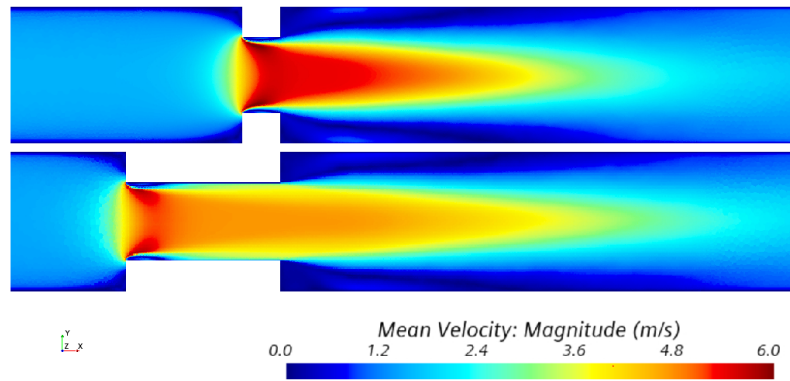
For both porosities the shapes of the flows are very similar, but the scale of the velocity varies for different porosities. This is as expected because a larger porosity orifice creates a lower velocity increase due to conservation of mass.

Q-criterion

One method of visualizing vortex structures in flow is by using the Q-criterion. The Q-criterion looks at the second invariant of the velocity gradient tensor, $\boldsymbol{Q}$. The Q-criterion defines a vortex as a connected fluid region with a positive second invariant of ∇u, i.e. $\boldsymbol{Q} > 0$ [54]. $\boldsymbol{Q}$ represents the local balance between shear strain rate and the vorticity magnitude, defining vortices as areas where the vorticity magnitude is greater than the magnitude of rate-of-strain [55]. Figure 5.16 shows two snapshots of the Q-criterion for a thin and a thick orifice of the same porosity.
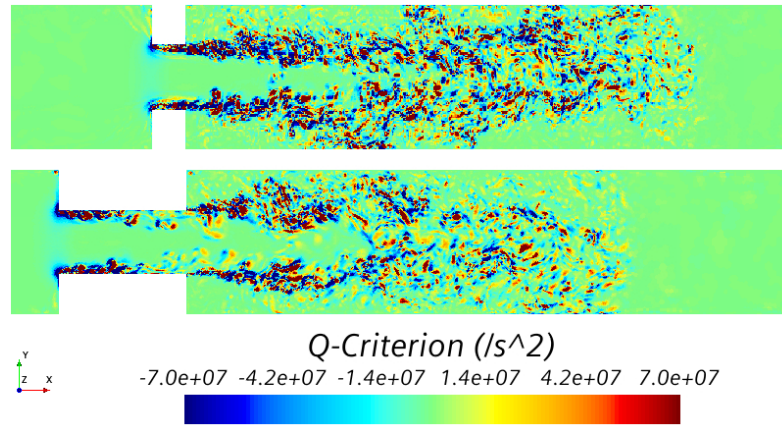

Figure 5.16: Snapshot of the Q-criterion for a thin and a thick orifice of $\beta = 20\%$ and a thickness ratio of 0.5 and 2 respectively

Differences between the thin and thick orifice are clearly visible. For the thin orifice the vortexes are generated at the inlet of the orifice and are transported through the orifice into the domain downstream. For the thick orifice the vortexes are also generated at the inlet of the orifice. However, they mostly dissipate as the flow reattaches within the orifice. This results in less vortex structures downstream of the orifice and less interaction between these structures. It is likely that the amount of vortex structures downstream of the orifice is correlated to the amount of acoustic force produced.

Lamb vector

Another method for visualizing the vortex structures in a fluid domain is using the lamb vector. The lamb vector is defined as:

$$\boldsymbol{\lambda} = \boldsymbol{\omega} \times \boldsymbol{u} \tag{5.1}$$

Where $\boldsymbol{\lambda}$ is the lamb vector, $\boldsymbol{\omega}$ is the vorticity vector and $\boldsymbol{u}$ is the velocity vector. The lamb vector is of particular interest because the fluctuating part of the lamb vector is used for extracting the force term from simulations as described in Section 4.2.2. Snapshots of the lamb vector for a thin and thick orifice are displayed in Figure 5.17.

Similar to the Q-criterion, the lamb vector for the thick orifice shows less vortex structures downstream of the orifice. However, for the lamb vector the vortex structures within the thick orifice do not fully break up as was visible for the Q-criterion. The mean lamb vector for a thick orifice of $\beta = 20\%$ and $t_o/d_o = 2$ can be seen in Figure 5.18.
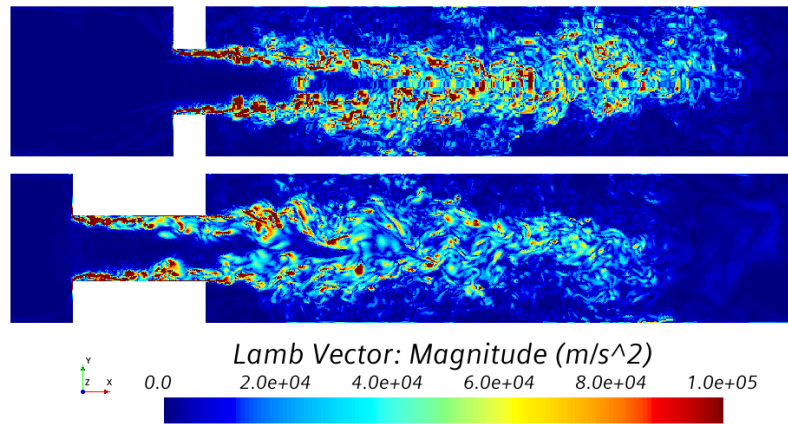
Figure 5.17: Side view cross sections of a snapshot of the lamb vector for a thin and a thick orifice of $\beta = 20\%$ and $t_o/d_o = 0.5$ and 2 respectively
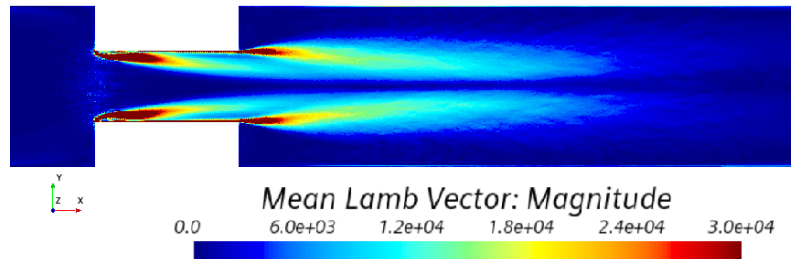
Figure 5.18: Side view cross section of the mean lamb vector for a thick orifice of $\beta = 20\%$ and $t_o/d_o = 0.5$

The mean of the lamb vector is a representation of the drag force generated by the orifice. The highest concentrations of force are located at the corners of the inlet of the orifice and the corners at the outlet of the orifice. This is where the flow experiences a sudden contraction and a sudden expansion. The force generating the FIV is described by the fluctuating part of the lamb vector.

5.2.3 Force

Extracting the acoustic force source term from the LES makes it possible to predict pressure fluctuations throughout the system. In this section the volume from which the force signal is extracted will be discussed as well as the influence of orifice geometry on the generated force source term.

Force control volume

The force signal is extracted from the simulation using the volume integral method as discussed in Section 4.2.2. In order to capture all the force created by the orifice, the correct control volume should be used. In order to find a suitable control volume, the force integral is taken over control volumes of increasing size. Figure 5.19 shows the PSDs of force signals taken from a LES of $\beta = 20\%$ and $t_o/d_o = 2$, using control volumes of increasing sizes.

(a) PSD comparison

(b) Visualisation of control volume sizes

Figure 5.19: Force PSDs for control volumes of increasing size, for an orifice of $\beta = 20\%$ and $t_o/d_o = 2$
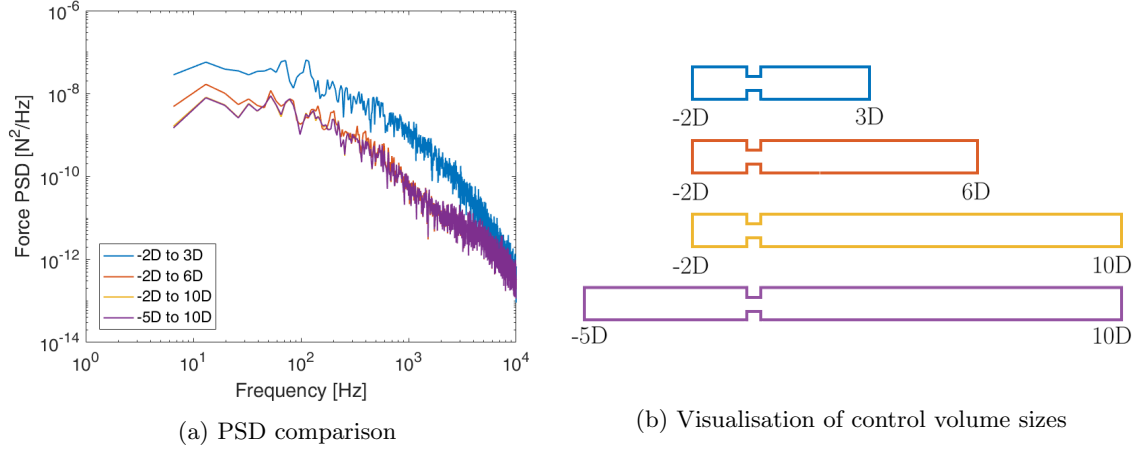
It was found that if the downstream boundary of the control volume is larger than $6D$, the shape of the PSD will not change significantly anymore. Increasing the size of the control volume in upstream direction does not cause any difference as long as the orifice is included in the control volume. This is in agreement with the expectation that vortex structures are formed within the orifice and directly downstream of the orifice. It can also be seen that the force PSD is decreasing as the control volume increases, which is counter-intuitive because it is expected that increasing the volume only adds to the force volume integral. Investigating this behaviour is done by splitting the control volume of $-2D$ to $6D$ into two sections. Figure 5.20 shows the PSD spectra and force signals of $-2D$ to $3D$ and $3D$ to $6D$.

(a) PSD comparison

(b) Force signal comparison
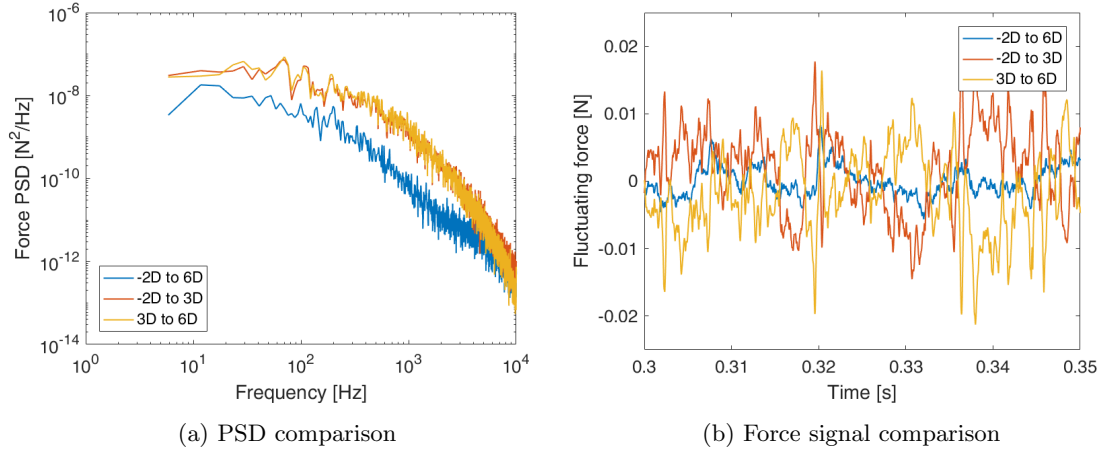
Figure 5.20: Comparison between the extracted forces of domains $-2D$ to $3D$ and $3D$ to $6D$, for an orifice of $\beta = 20\%$ and $t_o/d_o = 2$

It was found that the pressure PSDs of $-2D$ to $3D$ and $3D$ to $6D$ are nearly identical. Figure 5.20b shows the time signal of the fluctuating force. The force signals of the two control volumes are nearly mirror images of each other. This means that the force contribution downstream of $3D$ is mostly cancelling out the force contribution upstream of $3D$. The resulting force is therefor lower, which is reflected in the PSD in Figure 5.20a.

A simulation was carried out where the downstream control volume is split into smaller sections of $0.5D$. From the force signal of these smaller control volumes the RMS value is extracted and visualized in Figure 5.21.

Figure 5.21: Force RMS for increasing control volumes. The control volume used to calculate the RMS is from $x/D = -2$ to the value given on the x-axis, taken from a LES containing an orifice of $\beta = 20\%$ and $t_o/d_o = 2$

The RMS peaks right after the orifice and at a downstream boundary position of $x/D > 4$ it reaches its equilibrium. From this it is assumed that using a force signal of a volume from $-2D$ to $6D$ is sufficient.

Influence of geometry on force

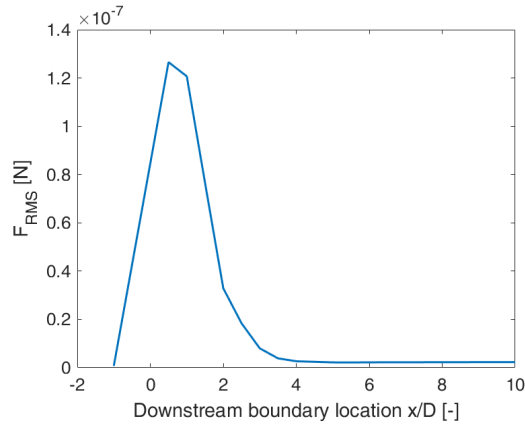LES were carried out for thick orifices of $\beta = 20\%$ and 31% and thickness to diameter ratios of $t_o/d_o = 2$ and 4. Simulations by Kottapalli [34] are used for thin orifice data. Those simulations were done for porosities of $\beta = 20\%$ and 31% and an orifice thickness to diameter ratio of 0.5. All simulations were carried out at similar bulk velocities with an equivalent bulk Reynolds number of approximately 12000. A comparison between the force PSDs extracted from the simulations for volumes of $-2D$ to $6D$ is shown in Figure 5.22. Figure 5.22a shows the original force PSDs and 5.22b shows the force PSDs scaled with the pressure drop squared. Scaling in this way shows the force per unit pressure drop, giving insight in the efficiency of orifice geometries.

The lower boundary of the frequency spectrum is determined by the duration at which the simulations were ran. Because not all simulations were carried out for the same amount of time, the starting frequencies differ. Figure 5.22a shows a similar relation for the force PSDs as what was previously seen for the pressure PSDs. The thick orifices of $t_o/d_o = 2$ and 4 show no obvious difference. The thin orifice shows a generally higher PSD over all frequencies for a thin orifice compared a thick orifice of the same porosity. The force PSDs are scaled with pressure drop, as shown in Figure 5.22b. Below 1000Hz the thick orifices of $\beta = 31\%$ show a higher PSD than those of $\beta = 20\%$. The thin orifice of porosity 20% also shows a generally higher PSD, but for the 31% orifice this is not clearly noticeable.

(a) Force PSD

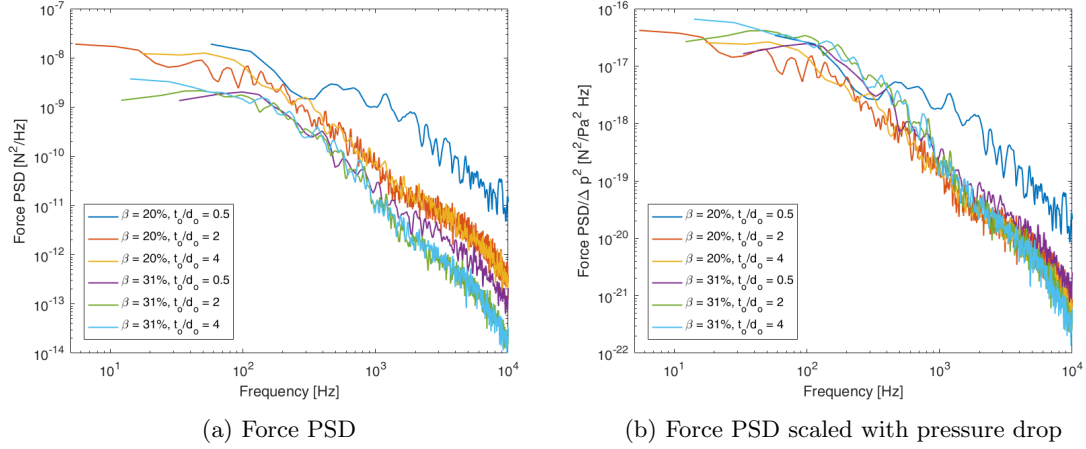(b) Force PSD scaled with pressure drop

Figure 5.22: Force PSD comparison for orifices of $\beta = 20\%$ and 31% of various thicknesses, extracted from the LES volume integral from -2D to 6D, $Re_b \approx 12000$

5.3 Measurement and simulation comparison

The measurement data and simulation data for validation purposes. If they match well, it can be concluded that the simulation is a good model for the real world application. The near field pressure fluctuation data can be compared directly because the pressure fluctuations can be measured and collected from the simulations at the same positions. Far field measurement data will be compared by using the force source term as an input and modeling far field pressure fluctuations using PlaNet3D.

5.3.1 Near field pressure

As discussed in Section 4.2 the pressure data from the simulations is averaged over a surface area comparable to the size of the area of the probe used in the real world measurements. The comparison of the pressure data between the measurements and the simulation of an orifice with $\beta = 20\%$ ($4mm$) and $t_o/d_o = 2$ is shown in Figure 5.23.

(a) x/D = 1

(b) x/D = 2

(c) x/D = 3
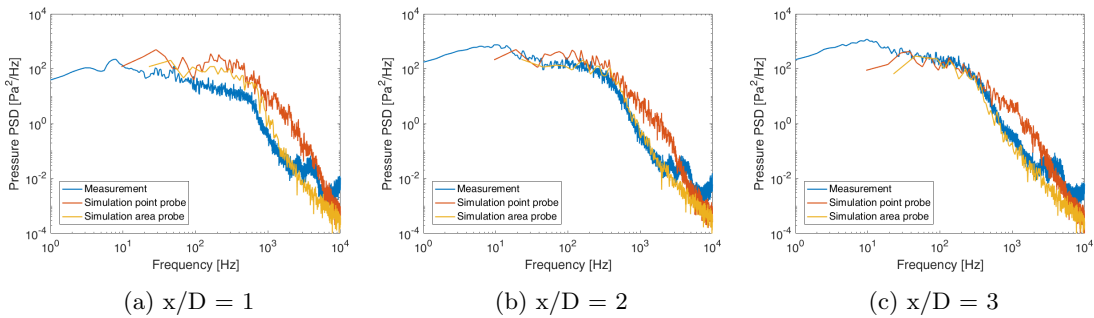
Figure 5.23: Comparison between measurements and simulations of the pressure PSD at various locations close to the orifice, for an orifice of $\beta = 20\%$ ($4mm$) and $t_o/d_o = 2$

The pressure PSDs of the measurements and area probes from the simulation show a good collapse up until $1000\ Hz$, which is within the region of interest. For higher frequencies the measurements hit a noise floor and are no longer comparable to the simulation. This validates that the pressure data from the simulations can be used to predict real life near field pressure fluctuations. Each of the figures show a clear difference between the point probe data and the

area probe data from approximately 600 Hz upward, as was discussed in Section 4.2.1. It should be noted that the results from the measurements and the area probe underpredict the actual pressure fluctuations due to surface averaging. This means that the actual forces that are transferred from the fluid domain to the structural domain are higher than previously assumed.

5.3.2 Far field pressure

For the far field pressure PSDs a comparison can be made between the measurements and the pressure output generated by the model using PlaNet3D. The force source term was extracted from the STAR-CCM+ simulations using a volume of $-2D$ to $6D$ and were then used in the PlaNet3D model. The force source term was then used to obtain a duct pressure input. Using the duct pressure input, the node pressure outputs were extracted and compared to the measurements. Figures 5.24 and 5.25 show the far field pressure PSD comparisons for thick orifices of $\beta = 2$ and porosities of $\beta = 20\%$ and 31% respectively.

(a) x/D = 142   (b) x/D = 172   (c) x/D = 283
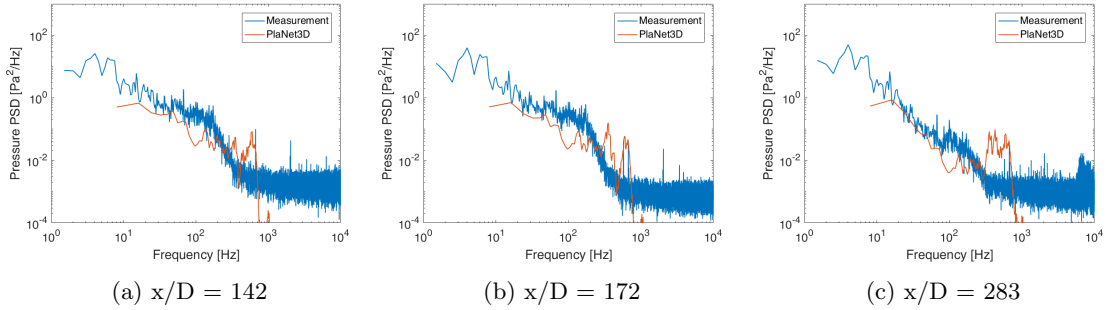
Figure 5.24: Comparison between measurements and PlaNet3D output of the pressure PSD at various locations far field form the orifice, for an orifice of $\beta = 20\%$ $(4mm)$ and $t_o/d_o = 2$

(a) x/D = 142   (b) x/D = 172   (c) x/D = 283
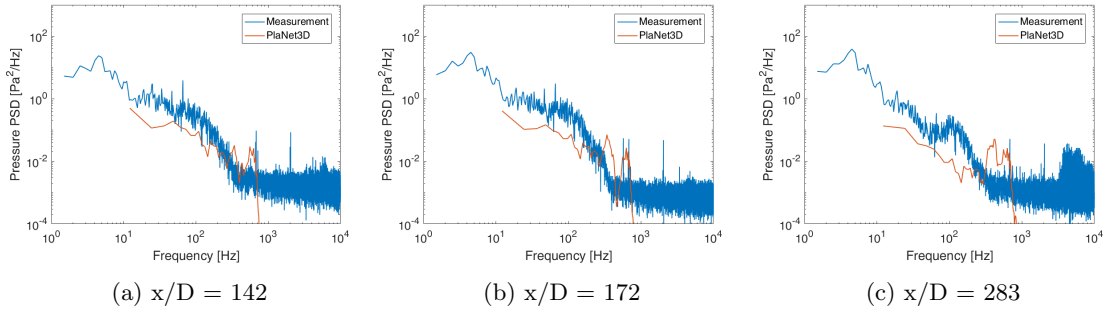
Figure 5.25: Comparison between measurements and PlaNet3D output of the pressure PSD at various locations far field form the orifice, for an orifice of $\beta = 31\%$ $(5mm)$ and $t_o/d_o = 2$

The measurements and output from the PlaNet3D model show a reasonable agreement for both porosities. The shape matches adequately, but between 100 and 1000Hz some peaks are introduced in the PSDs from the PlaNet3D model. It is unclear where these peaks originate from as they are not evident in the force PSD input. The PlaNet3D model generally underpredicts the pressure PSDs. Further investigation should be done on the PlaNet3D model itself.

Chapter 6

Conclusions and recommendations

In this chapter first conclusions will be made regarding the research done on orifice flow. Then some discussion and recommendations for further work based on the conclusions will be discussed.

6.1 Conclusions

A new orifice mount was machined to allow measurements with thin as well as thick orifices. Measurements were carried out using this new orifice mount and earlier results gathered with the old orifice mount were reproduced. This validates the use of the new orifice mount.

Pressure measurements were carried out in the near field and far field of the orifice for orifices of porosities $\beta = 20\%$ and $\beta = 31\%$ and thickness to diameter ratios of $t_o/d_o = 0.5$, 2 and 4. It was found that all PSDs for thickness to diameter ratios of 2 and 4 of the same porosity were nearly identical. For the near field pressure fluctuations it was found that for thin orifices the largest pressure fluctuations were measured at $x/D = 1$ and 2. For the thick orifices the largest pressure fluctuations in the near field were found at $x/D = 2$ and 3. Measurements were conducted at the same bulk velocity. The PSDs found in the near field and far field both showed that orifices of smaller porosity cause larger pressure fluctuations. They also showed that thin orifices cause larger pressure fluctuations than thick ones. The PSDs scaled with pressure drop showed agreement that 31% orifices generate higher PSDs per unit pressure drop than 20% orifices. It can be concluded that for a desired pressure drop it is best to use a single, low porosity orifice instead of multiple larger porosity orifices. It should be taken into consideration that only non-cavitating flows are considered.

LES were carried out in order to gain a better understanding of the flow mechanisms responsible for the pressure fluctuations. Also, a force source term used for far field pressure fluctuation modeling is extracted. Pressure fluctuations at locations near the orifice were extracted and scaled with pressure drop. In agreement with the measurements the simulation showed that higher porosity orifices show larger pressure fluctuations per unit pressure drop. The flow fields showed that for thick orifices the flow reattaches within the orifice. Less vortex structures were visible downstream of a thick orifice compared to a thin orifice. A force source term was extracted and also scaled with pressure drop. Again the forces per unit pressure drop were larger for larger porosity orifices.

When comparing near field pressure fluctuations from simulations and experiments, the area of the probe should be taken into account. In the simulations this was done by extracting the pressure signal using a surface averaged signal, where the surface represents the surface area of the pressure transducer. Using this method a good collapse was found between the near field pressure fluctuations from the simulations and experiments. Using point probes in the same locations shows that the PSDs using surface averaging underpredicts the maximum local pressure

fluctuations. This effect is mainly noticeable for frequencies higher than 600Hz. The maximum pressure fluctuations that are propagating from the fluid domain to the structural domain are therefor also underpredicted.

The far field pressure fluctuations were compared using pressure measurements from experiments and pressure fluctuations modeled using PlaNet3D. For the modeled pressure fluctuations the force source term extracted from LES was used. The modeled and measured far field pressure fluctuations are found to compare reasonably well. The shape of the modeled pressure PSDs matches the measured PSDs well up to 1000Hz, except for some peaks introduced around 800Hz. The modeled PSD magnitudes are underpredicted. The underprediction and peaks are most likely due to the way the damping is modeled in PlaNet3D. This method of modeling far field pressure fluctuations is promising, but improvements are needed to be able to accurately model reality.

6.2 Further work and recommendations

Based on the conclusions found in the previous section, some recommendations can be made. First, more measurements and simulations should be performed using thin and thick orifices of different porosities than used in this study. Using more data, a relation can be found for the pressure fluctuations and force source term caused by an orifice as a function of the porosity and thickness to diameter ratio. Using such a relation, it can be determined what the most efficient orifice is for a specific pressure drop, i.e. the orifice which induces the least amount of pressure fluctuations at that pressure drop. Next, other orifice geometries can be tested. For example, orifices with chamfered or rounded edges could be tested.. Also the pressure fluctuations caused by other components such as sudden bends or valves can be measured or simulated.

More work should be done on the far field modeling of pressure fluctuations. Once the modeled far field pressure fluctuations match with the measured pressure fluctuations, more complex models can be built to further validate the acoustic force source term. The force source term can then be scaled to predict pressure fluctuations of orifices of different geometries.

Bibliography

[1] I. Krabben, "Determination of the source term disturbing bounded flow performing practical large eddy simulations," Master's thesis, University of Twente, 2020. vii, 3, 11, 32

[2] J. McLoone, "Orifice plates & automatic sizing of orifice plates," 2019. vii, 5

[3] I. Idelchik, "Handbook of hydraulic resistance," *wdch*, 1986. vii, 5, 6, 7, 25, 52

[4] P. A. Davidson, *Turbulence: an introduction for scientists and engineers.* Oxford university press, 2015. vii, 8

[5] P. Grete, "Subgrid-scale modeling of mhd turbulence," 2021. vii, 8

[6] FLEXIM, *FLUXUS F601, Portable ultrasonic flow measurement of liquids*, 2020. vii, 14

[7] R. D. Blevins, "Flow-induced vibrations. reprint of the 1990," 2001. 3

[8] T. Nakamura, S. Kaneko, F. Inada, M. Kato, K. Ishihara, T. Nishihara, N. W. Mureithi, and M. A. Langthjem, *Flow-induced vibrations: classifications and lessons from practical experiences.* Butterworth-Heinemann, 2013. 3

[9] C. Moonen, "Experimental and numerical study on acoustic resonance in turbulent pipe-flow," Master's thesis, Eindhoven University of Technology, 2016. 3

[10] V. Anantharaman, "Characteristics of flow through orifices in pipes: an experimental investigation," Master's thesis, Delft University of Technology, 2014. 5, 10, 12, 25, 47

[11] R. Bird, W. E. Stewart, E. N. Lightfoot, and D. J. Klingenberg, *Introductory transport phenomena.* Wiley Global Education, 2015. 5

[12] S. B. Pope, "Turbulent flows," 2001. 6

[13] P. Kundu, D. Dowling, G. Tryggvason, and I. Cohen, "Fluid mechanics," 2015. 6

[14] D. Maynes, G. Holt, and J. Blotter, "Cavitation inception and head loss due to liquid flow through perforated plates of varying thickness," *Journal of fluids engineering*, vol. 135, no. 3, 2013. 6, 15

[15] J. Smagorinsky, "General circulation experiment with the primitive equations. monthly weather review," 1963. 7

[16] J. W. Deardorff *et al.*, "A numerical study of three-dimensional turbulent channel flow at large reynolds numbers," *J. Fluid Mech*, vol. 41, no. 2, pp. 453–480, 1970. 7

[17] B. Chaouat, "The state of the art of hybrid rans/les modeling for the simulation of turbulent flows," *Flow, turbulence and combustion*, vol. 99, no. 2, pp. 279–327, 2017. 7, 11

[18] L. F. Richardson, *Weather prediction by numerical process.* Cambridge university press, 2007. 7

[19] A. N. Kolmogorov, "The local structure of turbulence in incompressible viscous fluid for very large reynolds numbers," *Proceedings of the Royal Society of London. Series A: Mathematical and Physical Sciences*, vol. 434, no. 1890, pp. 9–13, 1991. 7

[20] J. Anderson, "Fundamentals of aerodynamics, chapter 2, 7, 15," 2016. 9

[21] M. J. Lighthill, "On sound generated aerodynamically i. general theory," *Proceedings of the Royal Society of London. Series A. Mathematical and Physical Sciences*, vol. 211, no. 1107, pp. 564–587, 1952. 9

[22] A. Powell, "Theory of vortex sound," *The journal of the acoustical society of America*, vol. 36, no. 1, pp. 177–195, 1964. 9

[23] A. Hirschberg, "Introduction to aero-acoustics of internal flows," in *Basics of aeroacoustics and thermoacoustics*, pp. 1–112, Von Karman Institute for Fluid Dynamics, 2007. 10

[24] N. Agarwal, "The sound field in fully developed turbulent pipe flow due to internal flow separation, part i: Wall-pressure fluctuations," *Journal of sound and vibration*, vol. 169, no. 1, pp. 89–109, 1994. 10

[25] M. Qing, Z. Jinghui, L. Yushan, W. Haijun, and D. Quan, "Experimental studies of orifice-induced wall pressure fluctuations and pipe vibration," *International journal of pressure vessels and piping*, vol. 83, no. 7, pp. 505–511, 2006. 10, 13, 17, 26

[26] P. Moussou, "An attempt to scale the vibrations of water pipes," 2006. 10, 17

[27] D. Violato, B. De Jong, and J. Golliard, "Universal scaling for broadband turbulent noise in internal flow devices," in *Proceedings of the 11th International Conference on Flow Induced Vibration and Noise, The Hague, Netherlands*, 2016. 10

[28] G. Moore, "Moore's law," *Electronics Magazine*, vol. 38, no. 8, p. 114, 1965. 10

[29] S. B. Pope, "Ten questions concerning the large-eddy simulation of turbulent flows," *New journal of Physics*, vol. 6, no. 1, p. 35, 2004. 10

[30] M. A. Siba, W. Mahood, Z. Nuawi, R. Rasani, and M. Nassir, "Modelling and applications of 3d flow in orifice plate at low turbulent reynolds numbers," *International Journal of Mechanical & Mechatronics Engineering IJMME-IJENS.*, vol. 15, no. 4, pp. 19–25, 2015. 11

[31] E. Alenius, *Flow duct acoustics: an LES approach.* PhD thesis, KTH Royal Institute of Technology, 2012. 11

[32] S. Benhamadouche, M. Arenas, and W. Malouf, "Wall-resolved large eddy simulation of a flow through a square-edged orifice in a round pipe at re= 25,000," *Nuclear Engineering and Design*, vol. 312, pp. 128–136, 2017. 11

[33] PCB Piezotronics, Inc, *Model 105C02 ICP® Pressure Sensor Installation and Operating Manual*, 2011. 13

[34] S. Kottapalli, "Near-filed pressure fluctuations in water pipes due to an orifice: Compariosn of measurements with large eddy simulations." Unpublished, 2021. 15, 18, 32, 38, 47

[35] M. Weik, *Computer science and communications dictionary.* Springer Science & Business Media, 2000. 16

[36] F. J. Harris, "On the use of windows for harmonic analysis with the discrete fourier transform," *Proceedings of the IEEE*, vol. 66, no. 1, pp. 51–83, 1978. 16

[37] A. de Jong and J. Golliard, "Towards a universal scaling for broadband turbulent noise in internal flow devices," in *ASME International Mechanical Engineering Congress and Exposition*, vol. 56437, p. V014T15A019, American Society of Mechanical Engineers, 2013. 17

[38] R.-J. Gibert, "Vibrations des structures," 1988. 17

[39] P. Testud, P. Moussou, A. Hirschberg, and Y. Aurégan, "Noise generated by cavitating single-hole and multi-hole orifices in a water pipe," *Journal of fluids and structures*, vol. 23, no. 2, pp. 163–189, 2007. 17

[40] P. Moussou, P. Testud, Y. Aure´ gan, and A. Hirschberg, "An acoustic criterion for the whistling of orifices in pipes," in *ASME Pressure Vessels and Piping Conference*, vol. 42827, pp. 345–353, 2007. 17

[41] R. J. Tobin and I.-D. Chang, "Wall pressure spectra scaling downstream of stenoses in steady tube flow," *Journal of Biomechanics*, vol. 9, no. 10, pp. 633–640, 1976. 17

[42] K. Maley, "Best practices: Volume meshing," 2012. 19

[43] N. Jarrin, S. Benhamadouche, D. Laurence, and R. Prosser, "A synthetic-eddy-method for generating inflow conditions for large-eddy simulations," *International Journal of Heat and Fluid Flow*, vol. 27, no. 4, pp. 585–593, 2006. 20

[44] F. Russo and N. T. Basse, "Scaling of turbulence intensity for low-speed flow in smooth pipes," *Flow Measurement and Instrumentation*, vol. 52, pp. 101–114, 2016. 20

[45] R. Courant, K. Friedrichs, and H. Lewy, "Über die partiellen differenzengleichungen der mathematischen physik," *Mathematische annalen*, vol. 100, no. 1, pp. 32–74, 1928. 21

[46] F. Nicoud and F. Ducros, "Subgrid-scale stress modelling based on the square of the velocity gradient tensor," *Flow, turbulence and Combustion*, vol. 62, no. 3, pp. 183–200, 1999. 21

[47] J. Ma, F. Wang, and X. Tang, "Comparison of several subgrid-scale models for large-eddy simulation of turbulent flows in water turbine," in *Fluid Machinery and Fluid Mechanics*, pp. 328–334, Springer, 2009. 21

[48] P. Gaskell and A. Lau, "Curvature-compensated convective transport: Smart, a new boundedness-preserving transport algorithm," *International Journal for numerical methods in fluids*, vol. 8, no. 6, pp. 617–641, 1988. 22

[49] R. Lueptow, "Transducer resolution and the turbulent wall pressure spectrum," *The Journal of the Acoustical Society of America*, vol. 97, no. 1, pp. 370–378, 1995. 22

[50] G. Corcos, "Resolution of pressure in turbulence," *The Journal of the Acoustical Society of America*, vol. 35, no. 2, pp. 192–199, 1963. 22

[51] W. Willmarth and F. Roos, "Resolution and structure of the wall pressure field beneath a turbulent boundary layer," *Journal of Fluid Mechanics*, vol. 22, no. 1, pp. 81–94, 1965. 22

[52] S. Rienstra and A. Hirschberg, "An introduction to acoustics," *Eindhoven University of Technology*, vol. 18, p. 19, 2004. 23

[53] N. Kemper, "PIR LCW dynamics - acceleration induced disturbances," 2014. 23

[54] V. Kolář, "Vortex identification: New requirements and limitations," *International journal of heat and fluid flow*, vol. 28, no. 4, pp. 638–652, 2007. 35

[55] J. Hunt, A. Wray, and P. Moin, "Eddies, stream, and convergence zones in turbulent flows pp 193–208," *Center for Turbulence Research Report CTR*, p. S88, 1988. 35

Appendix A

Orifice mount

A new orifice mount was designed based on the the setup used in previous work by Anantharaman [10] and Kottapalli [34]. The previously used orifice had sleight alignment issues, but the main reason for changing the setup was to accommodate for the testing of thick orifices as well as the previously tested thin orifices.

The orifice mount consists of two parts, a female and a male part which are fitted to each other and can be connected using M4 hex socket cap screws. A mechanical drawing for the male and the female orifice mounts can be seen in the next pages. The male part has a groove which allows an O-ring to be fitted, which provides a sealed connection. The male part also has a groove cut in the front which is used for alignment of the orifices. Both parts have an internal diameter of 9 mm, which matches the rest of the ducting and piping and an external diameter of 12mm which allows for easy connection using a connection nut. The female orifice mount has a chamfer at the side where the male orifice mount in inserted, which helps to guide the O-ring into the female part and ensure a good fit. The female part has four holes on the top, used to mount the pressure transducers at hole center locations of $x/D = 1, 2, 3$ and 6 from the outlet of the orifice.

In order to validate the new orifice mount, a comparison is made between the old orifice mount and new orifice mount using near field pressure measurements. Figure A.1 shows the pressure PSD's measured using the old and the new orifice mount.
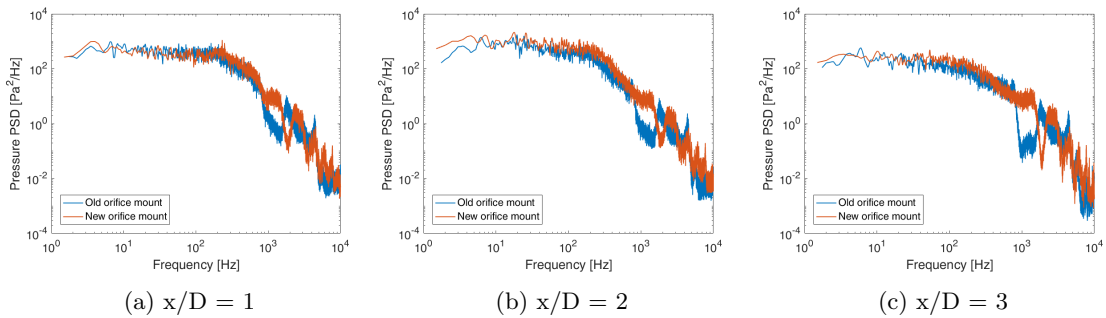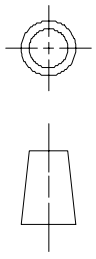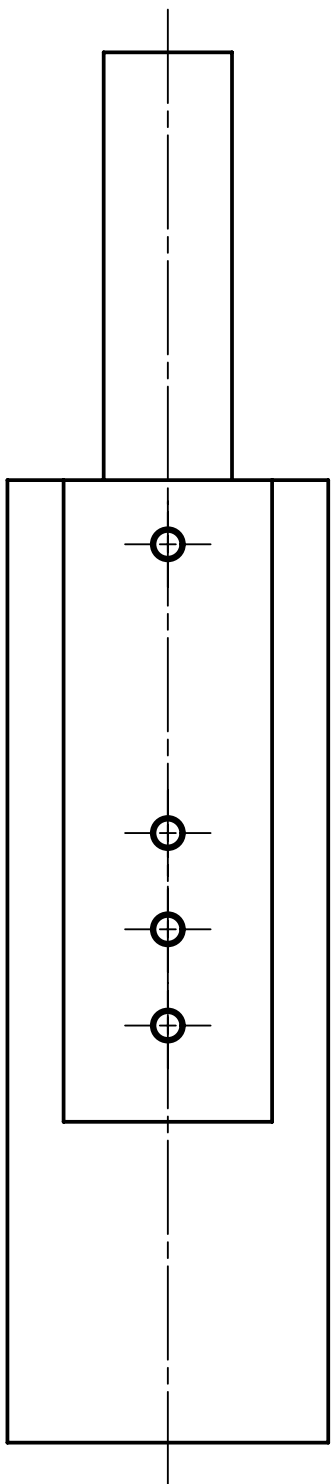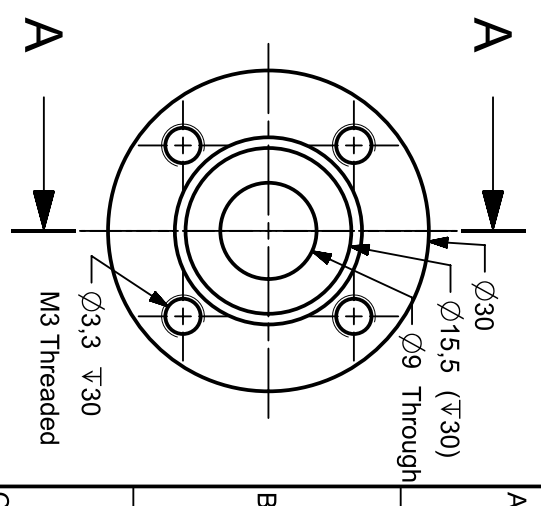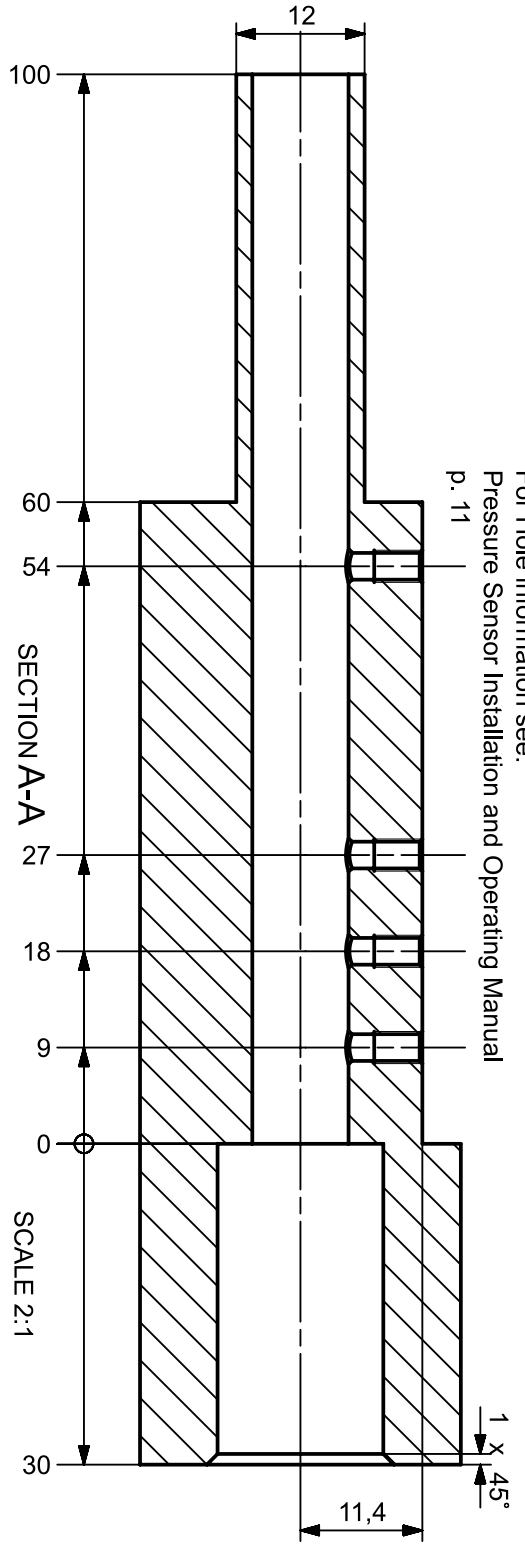

(a) x/D = 1   (b) x/D = 2   (c) x/D = 3

Figure A.1: Comparison between measurements taken using the old orifice mount and new orifice mount at various near field sensor locations

The only notable difference is the different peak frequencies for the high frequency domain, which are most likely due to difference in pipe length attached to the orifice mount used. It can be concluded that the new orifice mount is validated.

For Hole information see:
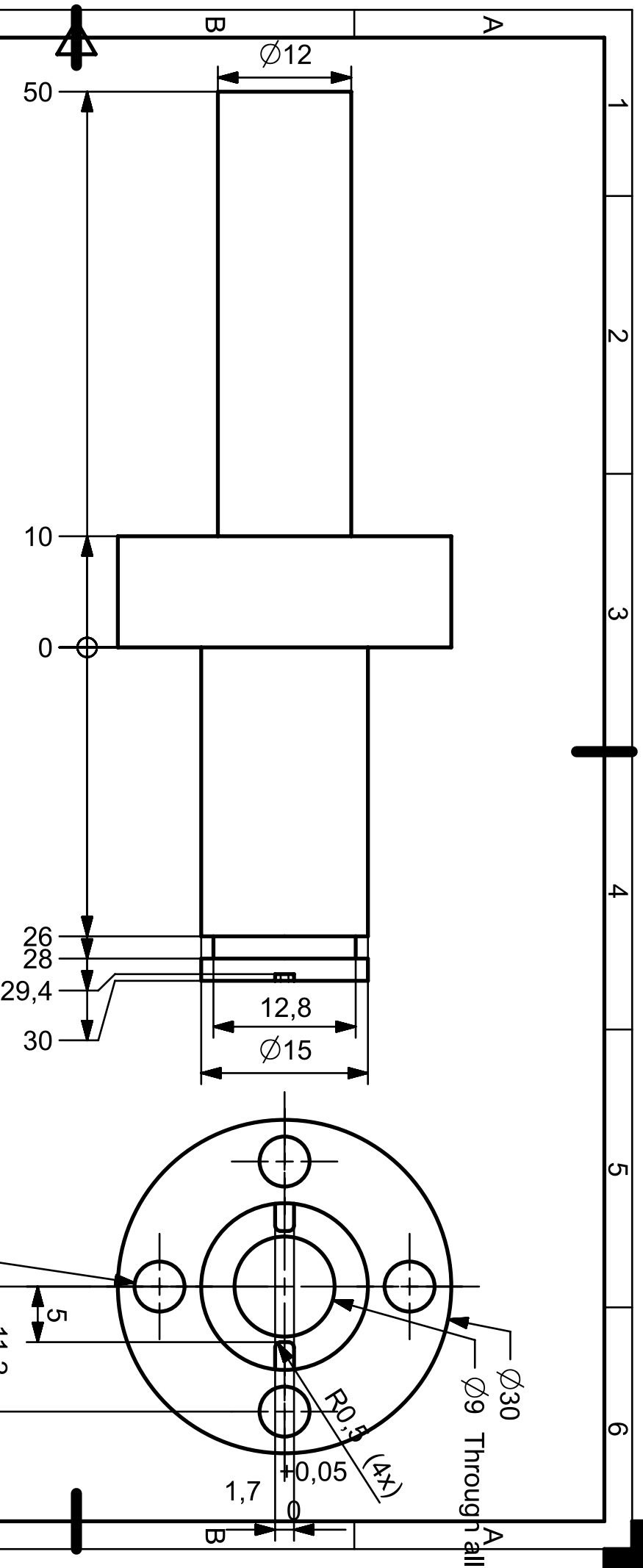Pressure Sensor Installation and Operating Manual
p. 11

SECTION A-A

SCALE 2:1

12

100

60

54

27

18

9

0

30

11,4

1 X 45°

∅30
∅15,5 (⌵30)
∅9 Through

∅3,3 ⌵30
M3 Threaded

A

A

ALL DIMENSIONS IN MM

SIEMENS

FIRST ISSUED	
DRAWN BY	L. Roumen
CHECKED BY	
APPROVED BY	

TITLE	Orifice Mount Female with sensor holes
SIZE	DRG NO.
A3	Orifice_Mount_Female_sensors_dwg1
SCALE 1:1	SHEET 1 OF 1

SHEET REV   A

A3

THIS DRAWING HAS BEEN PRODUCED USING AN EXAMPLE
TEMPLATE PROVIDED BY SIEMENS PLM SOFTWARE

ALL DIMENSIONS IN MM

Ø12

50

10

0

SCALE 2:1
M3 Screw Clearance

26
28
29,4
30

12,8

Ø15

Ø4,5 (4x)

5

11,2

Ø30

Ø9 Through all

R0,5 (4x)

1,7

+0,05
0

SIEMENS

FIRST ISSUED

DRAWN BY   L. Roumen

CHECKED BY

APPROVED BY

TITLE

Orifice Mount Male

SIZE   DRG NO.
A4   Orifice_Mount_dwg1

SCALE 1:1   SHEET 1 OF 1

A4   A

SHEET REV

THIS DRAWING HAS BEEN PRODUCED USING AN EXAMPLE
TEMPLATE PROVIDED BY SIEMENS PLM SOFTWARE

Appendix B

RANS simulations

A RANS simulation uses time-averaged equations of motion for the fluid flow. Since a RANS simulation only looks averaged quantities they generally solve quickly. RANS can be used to describe turbulent flow but does not contain the unsteady, time dependent behaviour that a LES can provide. Therefor RANS cannot be used to capture pressure fluctuations of force fluctuations in a system. RANS simulations can be used to predict mean flow fields and other associated means of parameters. Determining the initial mesh size needed is done by means of a RANS simulation. In order to find the mesh size that is used in LES, the Taylor microscale is used. At the Taylor microscale the viscosity of the fluid has a significant effect, as TKE starts to be dissipated into heat. A cross section of the Taylor microscale for an orifice of $\beta = 20\%$ and $t_o/d_o = 2$ can be seen in the figure below:
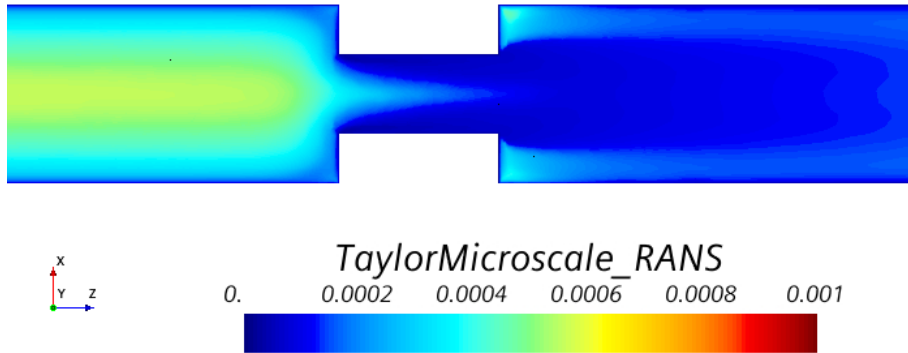

Figure B.1: Taylor microscale of a cross section extracted from a RANS simulation for an orifice of $\beta = 20\%$, $t_o/d_o = 2$ and $Re_b \approx 12000$

The Taylor microscale at the centerline of the bulk flow upstream of the orifice is found to be around 0.55mm. The mesh size for the bulk region in LES is therefor chosen at 0.45mm. The base cell size in the region $-1D\ to\ 3D$ is chosen at 20% of the bulk region base cell size, which is 0.09mm.

Appendix C

Near field and far field measurement comparison

In the main section of the report the near field pressure PSDs are compared to each other and likewise the far field pressure PSDs are compared. A complete overview of near field and far field pressure fluctuations is therefor given in Figure C.1.
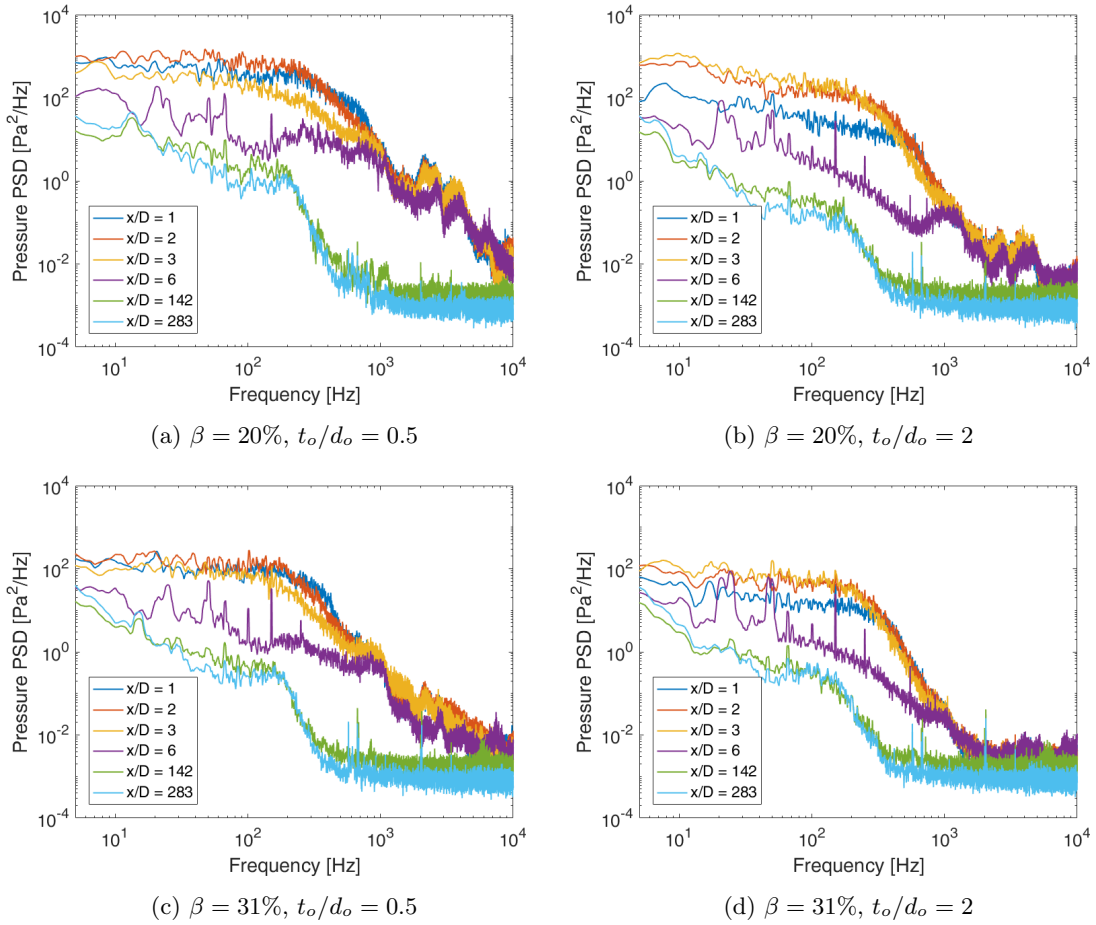

(a) $\beta = 20\%$, $t_o/d_o = 0.5$

(b) $\beta = 20\%$, $t_o/d_o = 2$

(c) $\beta = 31\%$, $t_o/d_o = 0.5$

(d) $\beta = 31\%$, $t_o/d_o = 2$

Figure C.1: Near field and far field pressure PSDs for thin and thick orifices

Appendix D

Thick orifice comparison

It is expected that the pressure drop over an orifice will not change more as the thickness increases after $t_o/d_o > 1.5$ [3]. Measurements were carried out with orifices of porosity $\beta = 20\%$ and 31% and thickness to diameter ratios of $t_o/d_o = 2$ and 4. The results of these near field pressure measurements can be found in the figure below:

(a) x/D = 1
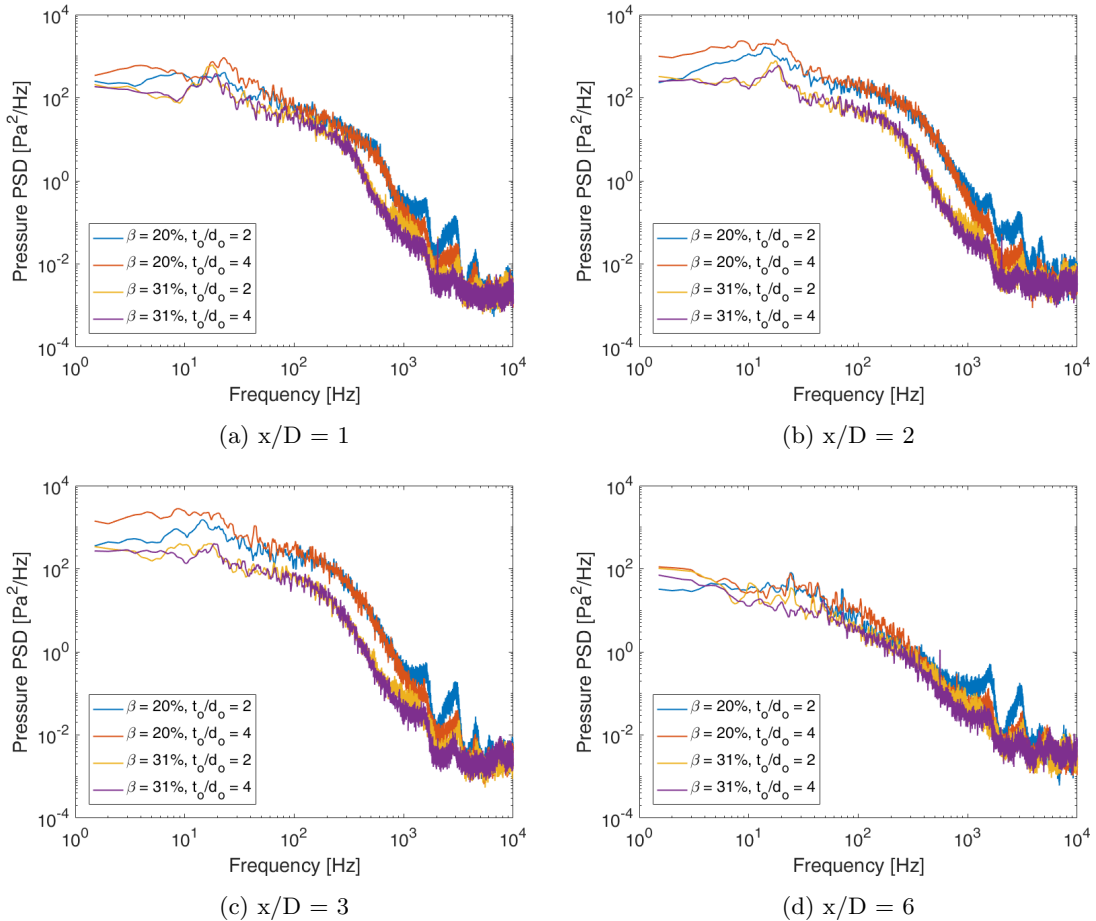
(b) x/D = 2

(c) x/D = 3

(d) x/D = 6

Figure D.1: Near field comparison of pressure PSD's for thick orifices of $\beta = 20\%$ and 31% (4 and 5mm)

Figure D.1 indeed shows that the difference between the different thick orifice for the same

porosities is negligible. The same comparison is made for far field pressure fluctuations of 20% orifices in Figure D.2 and 31% orifices in Figure D.3
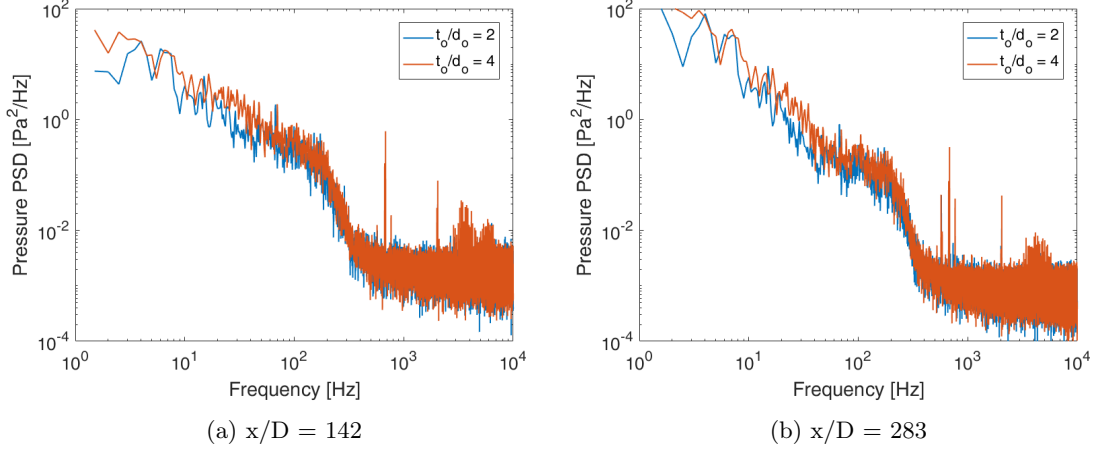

(a) x/D = 142　　　　　　　　　　　　　　　(b) x/D = 283

Figure D.2: Far field comparison of pressure PSD's for thick orifices of $\beta = 20\%$

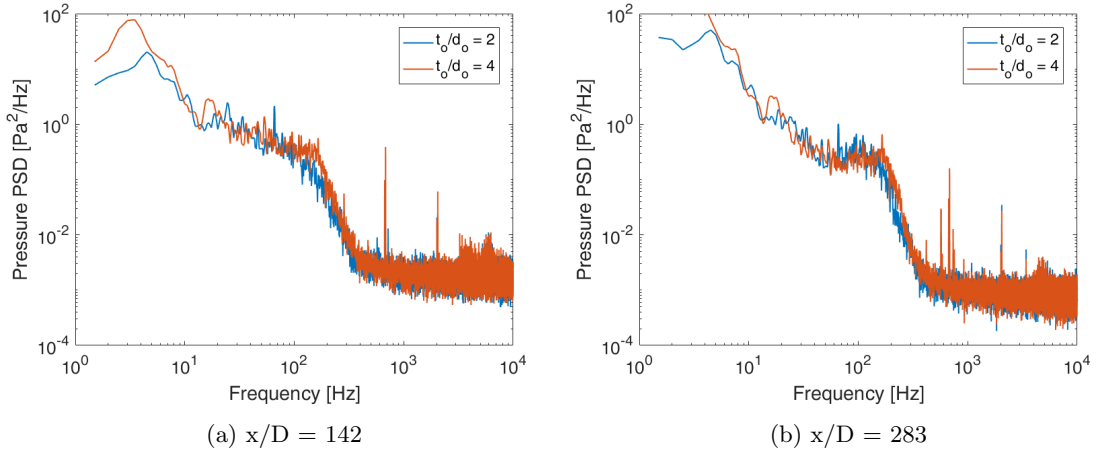(a) x/D = 142　　　　　　　　　　　　　　　(b) x/D = 283

Figure D.3: Far field comparison of pressure PSD's for thick orifices of $\beta = 31\%$

Again the PSD's are nearly identical for the different thicknesses. It is chosen to only include $t_o/d_o = 2$ in some of the comparisons with thick orifices.

Appendix E

Near field in line and Y-splitter comparison

In order to determine the influence of the Y-splitter setup for the near field pressure fluctuations a comparison is made. Figure E.1 shows the pressure PSD's for a thin orifice of porosity $\beta = 20\%$. Similar data was found for comparisons between thick orifices and orifices of porosity $\beta = 31\%$.

(a) x/D = 1   (b) x/D = 2   (c) x/D = 3
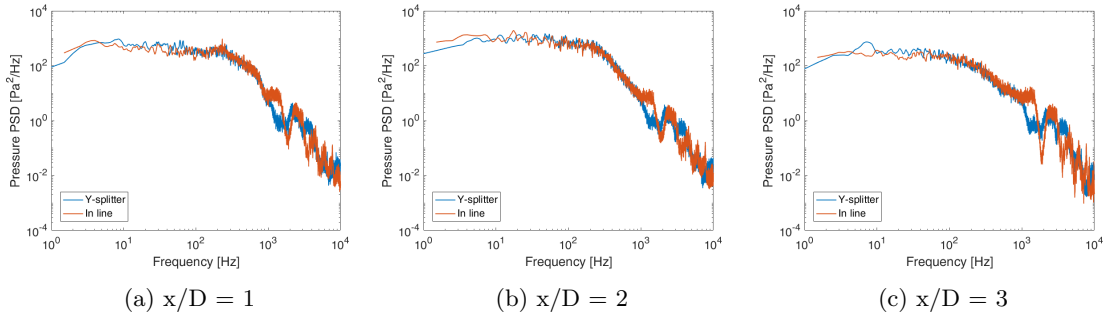
Figure E.1: Comparison between measurements taken using the in line setup and the Y-splitter setup at various near field sensor locations for an orifice of $\beta = 20\%$ and $t_o/d_o = 0.5$

From this figure it can be seen that the difference between the Y-splitter setup and in line setup for the near field pressure fluctuations is negligible. Especially the values for the low frequency ($f < 1000$Hz) the PSD's are almost identical. The difference in the higher frequencies is most likely due to the eigenfrequencies of the system being different due to the geometries being different. However, since the current focus is on the low frequency data and by far the largest contribution lies there, it is concluded that no significant difference is made in the near field pressure fluctuations due to the introduction of the Y-splitter.

Declaration concerning the TU/e Code of Scientific Conduct
for the Master's thesis

I have read the TU/e Code of Scientific Conduct[i].

I hereby declare that my Master's thesis has been carried out in accordance with the rules of the TU/e Code of Scientific Conduct

<u>Date</u>

12-02-2021
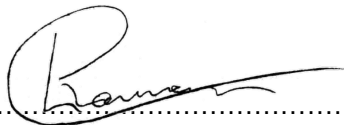……………………………………………..…………..

<u>Name</u>

Luuk Roumen
……………………………………………..…………..

<u>ID-number</u>

0900981
……………………………………………..…………..

<u>Signature</u>

……………………………………………..…………..

Submit the signed declaration to the student administration of your department.